This article has been accepted for publication in IEEE Transactions on Power Systems. This is the author's version which has not been fully edited and content may change prior to final publication. Citation information: DOI 10.1109/TPWRS.2026.3670426

Small-Signal Stability and Inertia Constrained Optimal Configuration Method of Grid-Forming Energy Storage Systems

Kezan Zhang, Xia Chen, *Senior Member*, *IEEE*, Yin Chen, Hui Yang, Huanhai Xin, *Senior Member*, *IEEE*, and Jinyu Wen, *Member*, *IEEE*

***Abstract*—With the increasing penetration of renewable energy sources and power electronic converters, the grid strength and inertia of modern power systems have significantly declined, potentially leading to various stability challenges, such as small-signal stability and frequency stability. It is widely recognized that the integration of grid-forming (GFM) energy storage systems (ESS) can mitigate these issues and enhance the stable operation of power systems from multiple perspectives. However, determining the optimal configuration of GFM ESS in hybrid systems to balance stability and economic efficiency remains an open research question. To bridge this gap, this paper proposes an optimization method for GFM ESS configuration considering stability constraints. First, based on the small-signal model of the multi-converter system, the relationship between system stability and the placement and capacity of GFM ESS is established, and stability criteria are derived. On this basis, both small-signal stability constraints and inertia constraints are incorporated, formulating the GFM ESS configuration problem as a mixed-integer programming problem. Finally, a relaxation method for eigenvalue constraints and a two-layer iterative algorithm are proposed to solve the optimization problem efficiently. Case studies conducted on the IEEE 39-bus system and the fully inverter-based system validate the accuracy and general applicability of the proposed configuration method.**

***Index Terms*—Optimal configuration, renewable power system, grid-forming energy storage systems, small-signal stability.**

I. Introduction

To achieve the zero-carbon target, renewable energy sources such as wind power and photovoltaic systems have been integrated into power systems on a large scale over the past decade [1]. In several regions, the penetration of renewable energy has exceeded 90%, as seen in South Australia and Ireland. Power electronic converters, serving as grid interfaces for renewable energy sources, significantly influence the stability and dynamic characteristics of power systems [2], [3]. Most existing power electronic converters operate under grid-following (GFL) control, synchronizing with the grid frequency through a phase-locked loop (PLL) [4]. However, with the decommission of synchronous generators (SGs), GFL converters face increasing synchronization stability challenges [5], which are particularly pronounced in high-renewable-penetration systems. In recent years, small-signal stability issues, such as sub-synchronous oscillations induced by weak grids, have attracted considerable attention [6]. Additionally, due to the control structure, GFL cannot provide an effective inertial response, leading to frequency stability concerns [7].

To mitigate stability issues caused by weak grids and low inertia, grid-forming (GFM) converters have been proposed as a viable alternative power source due to their dynamic characteristics similar to those of SGs [8]. GFM converters can autonomously establish system voltage and frequency while exhibiting a slowly varying internal voltage, significantly enhancing the small-signal stability of GFL converters [9], [10]. Furthermore, the virtual synchronous machine (VSM) control within GFM converters provides a rapid inertial response, effectively supporting system frequency stability [11]. It is now widely recognized that integrating GFM converters into power systems is the most promising solution for achieving these functionalities. Moreover, energy storage systems (ESS) are considered the most beneficial energy source for GFM converters due to their greater flexibility in deployment and operation [12].

The primary purpose of early ESS design was to address short-term and long-term power balance issues caused by the variability of renewable generation, such as peak shaving and frequency regulation. This objective also represented the main focus of most early studies on energy storage deployment [13], [14], [15]. With the advancement of grid-forming technology, GFM ESS has been widely deployed in renewable power systems, providing energy services while enhancing system robustness. Hybrid power systems comprising GFL renewable generation, GFM ESS, and SGs are expected to remain prevalent for the foreseeable future [16].

In recent years, theories and tools for analyzing the stability of hybrid power systems have been increasingly refined [17], [18], and scholars have increasingly focused on how to optimally configure GFM devices to enhance the stability of

This work was supported by the National Key Research and Development Program (No. 2023YFB2406600), and the National Natural Science Foundation of China (No. U24B6008). Paper no. TPWRS-00718-2025 (*Corresponding author: Xia Chen.*)

Kezan Zhang, Xia Chen, Hui Yang, and Jinyu Wen are with the College of Electrical and Electronic Engineering, Huazhong University of Science and Technology, Wuhan 430074, China (email: zhangkezan@hust.edu.cn, cxhust@hust.edu.cn, yanghui@hust.edu.cn, jinyu.wen@hust.edu.cn)

Yin Chen is with the Department of Electronic and Electrical Engineering, University of Strathclyde, Glasgow G1 1XW, U.K. (e-mail: yin.chen.101@strath.ac.uk.)

Huanhai Xin is with the College of Electrical Engineering, Zhejiang University, Hangzhou 310027, China (e-mail: xinhh@zju.edu.cn).

hybrid systems. Based on participation factors and power flow analysis, ref. [19] optimized the placement and capacity of GFM converters under voltage and power flow constraints. However, since the approach involves the configuration of a single GFM converter, it may lack general applicability. Ref. [20] proposed a greedy algorithm to determine the placement of GFM converters that maximizes grid strength. However, this approach requires repeatedly solving optimization problems involving eigenvalues, which may result in a computational burden. Additionally, it does not consider the capacity of the GFM converters. After analyzing the impedance model of the GFM converters, ref. [21] investigated the required proportion of GFM ESS to maintain small-signal stability based on the concept of generalized short-circuit ratio. However, it is assumed that the same proportion of GFM ESS was installed near all GFL converters, which may not be the most cost-effective solution in practice.

The existing studies on the configuration methods of GFM ESS exhibit several notable limitations: 1) They fail to account for the influence of GFM control parameters on the stability of GFL converters, which may lead to inaccurate results [22]; 2) They do not address stability issues intrinsic to the GFM converters themselves, resulting in configuration schemes that may not ensure the overall system stability [23]. For instance, in [24] and [25], GFM are simplified as a voltage source in series with an inductance during the configuration process, neglecting their inherent dynamic behavior. To fill these gaps, this paper extends the investigation of the placement, capacity, and inertia configuration of GFM ESS within hybrid systems, aiming to minimize configuration costs while maintaining system stability. Initially, based on the modeling and stability analysis of the hybrid GFL-GFM system, stability criteria for both GFL and GFM converters are derived. Subsequently, by incorporating constraints such as small-signal stability and inertia, the configuration problem is formulated as a mixed-integer programming (MIP) problem, with eigenvalue constraints subjected to a relaxation process. Finally, a two-layer iterative algorithm is proposed to solve the problem, and case studies are conducted on the IEEE 39-bus system. To evaluate the feasibility of GFM ESS independently supporting the operation of a renewable energy power system, the case study of a fully inverter-based system is also presented. The main contributions of this paper are summarized as follows:

1) Based on system partitioning and decoupling, the stability problem of a complex hybrid system is transformed into the stability analysis of a single equivalent converter. Furthermore, a small-signal stability criterion for the system is proposed. This criterion fully considers the impact of control parameters and strategies on system stability and the instability dominated by GFM themselves, leading to more accurate configuration results.
2) The configuration problem for GFM ESS is formulated based on a MIP approach, where the placement of GFM is represented by binary variables, thereby eliminating the computational burden associated with placement permutations. On this basis, an eigenvalue constraint relaxation method is proposed for different scenarios based on matrix differentiation theory, enabling the optimization problem to be solvable using existing solvers.
3) A capacity-inertia two-layer iterative algorithm is proposed, where the inner-layer iteration optimizes the placement and capacity, and the outer-layer iteration optimizes the inertia of GFM ESS. The two layers iteratively update data. This algorithm avoids the complex nonlinear constraints in the optimization problem, thereby enhancing the solution efficiency.

The rest of this paper is organized as follows: In Section II, the impedance model of the hybrid system is established, and a stability assessment method is proposed. Section III formulates the optimization configuration problem of GFM ESS under stability constraints. Section IV presents the solution method for the configuration problem. Case studies are provided in Section V. Section VI concludes the paper.

II. Modeling and Stability Assessment of the Multi-Converter System

This section first establishes the small-signal model of the hybrid system consisting of GFL and GFM converters based on the impedance method. The interaction dynamics between GFM and GFL converters are further clarified, and a stability assessment method for the system is proposed. These studies provide the foundation for formulating the GFM configuration problem in Section III.

A. Impedance Model of the Hybrid System

The schematic diagram of a hybrid power system is shown in Fig. 1, which includes n GFL converter nodes $\{1,2,\ldots,n\}$, m GFM converter nodes $\{n+1,\ldots,n+m\}$ and k internal nodes $\{n+m+1,\ldots,n+m+k\}$. Node 0 represents the infinite bus, which serves as the common grounded node. For economic considerations, the nodes to be configured with GFM are located at the high-voltage side of the GFL step-up transformers in the internal nodes [21]. The specific placements and capacities of the GFM converters will be determined by the optimization results. The impedance model of the system is established to characterize its stability, which includes the GFL converters, GFM converters, and the passive network.

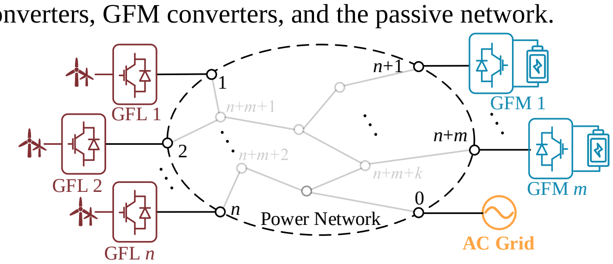

Fig. 1 Illustration of a hybrid power system.

1) Admittance model of the GFL converters

The admittance of the GFL Converters can be expressed as

$$\Delta \mathbf{I}_{GFL,i} = -S_{GFL,i} e^{J\theta_i} \mathbf{Y}_{GFL,i}(s) e^{-J\theta_i} \Delta \mathbf{U}_i,\ i = 1,2,\cdots n \quad (1)$$

where $\Delta \mathbf{I}_{GFL,i} = [\Delta I_{GFLd,i}, \Delta I_{GFLq,i}]^T$ and $\Delta \mathbf{U}_i = [\Delta U_{d,i}, \Delta U_{q,i}]^T$ are the vectors of the output current and terminal voltage of GFL converter i in the global reference frame. Δ denotes the

This article has been accepted for publication in IEEE Transactions on Power Systems. This is the author's version which has not been fully edited and content may change prior to final publication. Citation information: DOI 10.1109/TPWRS.2026.3670426

perturbed value of a variable. $S_{GFL,i}$ is the per-unit value of the capacity of the i-th GFL. $\mathbf{Y}_{GFL,i}(s)$ is the 2×2 admittance matrix in the frequency domain for the GFL converter with unit capacity, and its specific expression can be found in [26]. Matrix $e^{J\theta_i}=[\cos\theta_i\ \sin\theta_i;\ \sin\theta_i\ \text{-}\cos\theta_i]$ and θ_i represents the steady-state angle difference between the local dq reference frame of the i-th converter and the global reference frame. When the control strategies and parameters of the GFL within the system are homogeneous, all $\mathbf{Y}_{GFL,i}(s)$ in (1) are identical.

2) Impedance model of the GFM converter

When addressing small-signal stability concerns, GFM converters can be represented by a Thevenin equivalent circuit in the dq reference frame. Specifically, this model comprises an ideal voltage source and an internal impedance. The internal impedance $\mathbf{Z}_{\text{GFM}}(s)$, which is determined by the control strategy and parameters of the GFM converter, can be expressed as the sum of two independent impedances [27].

$$\begin{aligned}&\mathbf{Z}_{GFM}(s)=Z_{dq}(s)\boldsymbol{\alpha}(s)+\mathbf{Z}_{PF}(s)\\&Z_{dq}(s)=\frac{\omega_0 L_f}{H_V(s)},\ \boldsymbol{\alpha}(s)=\begin{bmatrix} s/\omega_0 & -1\\ 1 & s/\omega_0\end{bmatrix}\\&\mathbf{Z}_{PF}(s)\approx\omega_0 H_{PSC}\begin{bmatrix}0&0\\V_{d0}^2&0\end{bmatrix},\ H_{PSC}(s)=\frac{1}{Js^2+Ds}\end{aligned}\tag{2}$$

where $Z_{dq}(s)\boldsymbol{\alpha}(s)$ represents the impedance generated by the inner-loop control of the GFM, L_f is the filtering inductance, $H_V(s)=PI_{\text{VCL}}(s)PI_{\text{CCL}}(s)$, $PI_{\text{VCL}}(s)=K_{pv}+K_{iv}/s$, and $PI_{\text{CCL}}(s)=K_{pc}+K_{ic}/s$ are the transfer functions of the voltage and current PI controllers, respectively; $\mathbf{Z}_{\text{PF}}(s)$ is the impedance generated by the power synchronization loop; J and D are the inertia and damping coefficients, respectively. V_{d0} represents the steady-state values of the d-axis voltage.

Equation (2) describes a basic GFM control strategy, while in practice, several additional control loops of importance may also be incorporated. If the GFM converter adopts Q-V droop control, the corresponding impedance introduced by this control should also be incorporated into the expression of $\mathbf{Z}_{\text{GFM}}(s)$, denoted as $\mathbf{Z}_{\text{QV}}(s)$:

$$\mathbf{Z}_{QV}(s)=\begin{bmatrix}0 & -V_{d0}/D_q\\ 0 & 0\end{bmatrix}\tag{3}$$

where D_q denotes the reactive power droop coefficient.

When an additional damping control is applied to the GFM converter, an extra frequency-feedback branch is introduced in the active power control [28]. Consequently, the original damping coefficient D is replaced by the equivalent damping coefficient D_{eq}:

$$D_{eq}(s)=D+K_\omega\cdot\frac{sT_w}{1+sT_w}\cdot\frac{1+sT_1}{1+sT_2}\tag{4}$$

where K_ω is the additional damping gain, T_w is the time constant of the high-pass filter, T_1 and T_2 are the time constants of the phase compensator. There are various forms of additional damping control, and (4) is considered as a typical example in this paper.

The impedance model of the GFM converter can be described as:

$$\Delta\mathbf{U}_i=-e^{-J\theta_i}\frac{\mathbf{Z}_{GFM,i}(s)}{S_{GFM,i}}e^{J\theta_i}\Delta\mathbf{I}_{GFM,i},\ i=n+1,\cdots n+m.\tag{5}$$

where $\Delta\mathbf{I}_{GFM,i}=[\Delta I_{GFMd,i},\ \Delta I_{GFMq,i}]^T$ and $\Delta\mathbf{U}_i=[\Delta U_{d,i},\ \Delta U_{q,i}]^T$ are the vectors of the output current and terminal voltage of GFM converter i in the global reference frame. $S_{GFM,i}$ is the per-unit value of the capacity of the i-th GFM.

3) Model of the passive networks

When considering a general setting, the dynamic equation of the line between Node i and Node j is

$$\begin{bmatrix}\Delta I_{d,ij}\\ \Delta I_{q,ij}\end{bmatrix}=\mathbf{Y}_{ij}(s)\left(\begin{bmatrix}\Delta U_{d,i}\\ \Delta U_{q,i}\end{bmatrix}-\begin{bmatrix}\Delta U_{d,j}\\ \Delta U_{q,j}\end{bmatrix}\right)\tag{6}$$

where $[\Delta I_{d,ij},\ \Delta I_{q,ij}]^{\text{T}}$ is the vector of current between nodes i and j, and $\mathbf{Y}_{ij}(s)$ is a 2 × 2 transfer function matrix encoding the dynamics of the line. For the line composed of a resistor and an inductor, we have:

$$\mathbf{Y}_{ij}(s)=B_{ij}\begin{bmatrix}(s+\tau_{ij})/\omega_0 & -1\\ 1 & (s+\tau_{ij})/\omega_0\end{bmatrix}^{-1}=B_{ij}\mathbf{F}_{ij}(s)\tag{7}$$

where B_{ij} and τ_{ij} are the line susceptance and the R/X ratio of the line ij. For simplicity, the R/X ratio of all lines is assumed to be consistent (averaged), i.e., $\mathbf{F}_{ij}(s)=\mathbf{F}(s)$, $i, j = 0,1,\ldots,m+n+k$.

The network topology and admittance of the system are represented by the node Laplace matrix $\mathbf{B}$, with elements given by: $\mathbf{B}_{ij}=\text{-}B_{ij}$ $(i\neq j)$ and $B_{ii}=\sum_{j=1}^{m+n+k}B_{ij}$. By performing Kron reduction on $\mathbf{B}$, the Laplace matrix $\mathbf{B}_r$, which eliminates the internal nodes $\{n+m+1,\ \ldots,\ n+m+k\}$, can be obtained:

$$\mathbf{B}_r=\mathbf{B}_1-\mathbf{B}_2\mathbf{B}_4^{-1}\mathbf{B}_3\quad \mathbf{B}=\begin{bmatrix}\mathbf{B}_1\in\mathbb{R}^{(m+n)\times(m+n)} & \mathbf{B}_2\in\mathbb{R}^{(m+n)\times k}\\ \mathbf{B}_3\in\mathbb{R}^{k\times(m+n)} & \mathbf{B}_4\in\mathbb{R}^{k\times k}\end{bmatrix}\tag{8}$$

By combining (6), (7) and (8), the dynamics of the passive network can be described by the following $2(m+n)\times2(m+n)$ transfer function matrix.

$$\mathbf{I}_{dq}=\mathbf{Y}_{grid}(s)\mathbf{U}=\left[\mathbf{B}_r\otimes\mathbf{F}(s)\right]\mathbf{U}_{dq}\tag{9}$$

where $\mathbf{I}_{dq}=[I_{d,1},\ I_{q,1},\ldots,\ I_{d,m+n},\ I_{q,m+n}]^T$, $\mathbf{U}_{dq}=[U_{d,1},\ U_{q,1},\ldots,\ U_{d,m+n},\ U_{q,m+n}]^T$ are the injected current and voltage vectors of Node $\{1,2,\ldots,m+n\}$.

Equation (1), (5) and (9) establish the closed-loop dynamics of the multi-converter system, with its closed-loop characteristic equation given by:

$$\det\left(\left(\begin{bmatrix}\mathbf{S}_{GFL} & \\ & \mathbf{S}_{GFM}\end{bmatrix}\otimes\mathbf{I}_2\right)e^{J\Theta}\mathbf{Y}_C(s)e^{-J\Theta}+\mathbf{B}_r\otimes\mathbf{F}(s)\right)=0\tag{10}$$

where $\mathbf{S}_{GFL}=\text{diag}\{S_{\text{GFL},1},\ldots,S_{\text{GFL},n}\}$, $\mathbf{S}_{GFM}=\{S_{\text{GFM},1},\ldots,S_{\text{GFM},m}\}$ consist of the power ratings of each GFL and GFM converters. $\mathbf{Y}_C(s)=\text{diag}\{\mathbf{Y}_{\text{GFL},1}(s),\ldots,\ \mathbf{Y}_{\text{GFL},n}(s),\ \mathbf{Z}_{\text{GFM},1}^{-1},\ldots,\mathbf{Z}_{\text{GFM},m}^{-1}\}$ is the admittance matrix of all converters. $e^{J\Theta}=\text{diag}\{e^{J\theta_1},\ldots,e^{J\theta_{m+n}}\}$ is the reference frame transformation matrix.

B. Stability Assessment Method of the Hybrid System

1) System partitioning and decoupling

In Section II.A, the closed-loop dynamics of the multi-converter system are derived by separating the dynamics of the converters and the passive network, providing a foundation for system stability assessment. Given that GFM converters exhibit characteristics similar to voltage sources, they can be incorporated into the passive network to form an equivalent network [29], thereby partitioning the original system into two subsystems.

Proposition II.1: The hybrid system described with (10) is stable if the following two subsystems (characteristic equation) are both stable:

$$\begin{aligned}&\text{subsystem1: } \det\left(\mathbf{Y}_{C1}(s)\mathbf{Y}_{g,eq}^{-1}(s)+\mathbf{I}_{2n}\right)=0\\&\text{subsystem2: } \det\left(\mathbf{Y}_{C2}(s)\mathbf{Y}_{g4}^{-1}(s)+\mathbf{I}_{2m}\right)=0\end{aligned} \tag{11}$$

where:

$$\begin{aligned}&\begin{bmatrix}\mathbf{Y}_{C1}(s) & \\ & \mathbf{Y}_{C2}(s)\end{bmatrix}=\left(\begin{bmatrix}\mathbf{S}_{GFL} & \\ & \mathbf{S}_{GFM}\end{bmatrix}\otimes\mathbf{I}_2\right)e^{J\Theta}\mathbf{Y}_C(s)e^{-J\Theta}\\&\begin{bmatrix}\mathbf{Y}_{g1}(s) & \mathbf{Y}_{g2}(s)\\ \mathbf{Y}_{g3}(s) & \mathbf{Y}_{g4}(s)\end{bmatrix}=\begin{bmatrix}\mathbf{B}_{r1} & \mathbf{B}_{r2}\\ \mathbf{B}_{r3} & \mathbf{B}_{r4}\end{bmatrix}\otimes\mathbf{F}(s)=\mathbf{B}_r\otimes\mathbf{F}(s)\\&\mathbf{Y}_{g,eq}(s)=\mathbf{Y}_{g1}(s)-\mathbf{Y}_{g2}(s)\left[\mathbf{Y}_{C2}(s)+\mathbf{Y}_{g4}(s)\right]^{-1}\mathbf{Y}_{g3}(s)\end{aligned} \tag{12}$$

The dimensions of $\mathbf{Y}_{C1}(s)$ and $\mathbf{Y}_{C2}(s)$ are $2n\times2n$ and $2m\times2m$, respectively, while $\mathbf{Y}_{g1}(s)$ and $\mathbf{Y}_{g4}(s)$ have corresponding dimensions. $\mathbf{Y}_{g,eq}(s)$ represents the transfer function matrix of the equivalent network after the integration of the GFM converters.

Proof: See Appendix A.

From (11) and (12), it can be observed that if each GFM converter is sequentially replaced by an ideal voltage source in series with an impedance branch $\mathbf{Z}_{GFM,i}(s)/S_{GFM,i}$, the resulting system, which consists of n GFL converters, corresponds to subsystem 1 in (11). Since the GFM converters are equivalently modeled, the characteristic equation of subsystem 1 primarily reflects the stability characteristics dominated by the GFL converters.

The characteristic equation of subsystem 2 can be further expressed as (13), indicating that subsystem 2 represents a system consisting solely of m interconnected GFM converters after disconnecting the GFL branches. Consequently, the characteristic equation (13) characterizes the stability dominated by the GFM converters.

$$\det\left(\begin{bmatrix}\mathbf{0}_{2n} & \\ & \mathbf{Y}_{C2}(s)\end{bmatrix}+\mathbf{B}_r\otimes\mathbf{F}(s)\right)=0 \tag{13}$$

Compared to directly analyzing the original system, we partition the system into two subsystems, as illustrated in Fig. 2. Each subsystem contains only a single type of converter. Clearly, the stability of the original system is equivalent to the stability of both subsystems.

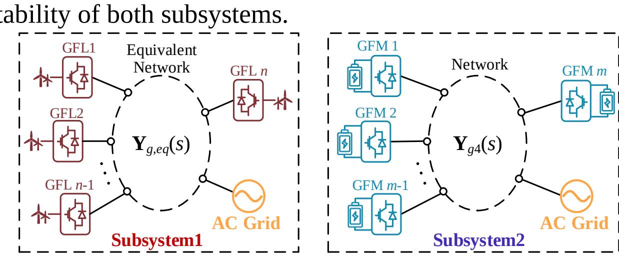

Fig. 2 Equivalent subsystems of the hybrid system

Typically, the impact of the steady-state power angle difference of converters on system small-signal stability is minor and can be neglected [20]. Thus, it follows that $e^{J\Theta}\approx e^{-J\Theta}\approx\mathbf{I}$. Additionally, it is assumed the control strategies and parameters of the GFM converters are homogeneous, i.e., $\mathbf{Z}_{GFM,i}(s)=\mathbf{Z}_{GFM}(s)$, $i=1,\ldots,m$. Based on the modal decoupling theory [18], subsystem 2, which consists of multiple GFM converters, can be decoupled into a series of single-converter-infinite-bus systems, where the grid-connected admittances correspond to the eigenvalues $\sigma_1, \sigma_2,\ldots,\sigma_m$ of matrix $\mathbf{S}_{\mathrm{GFM}}^{-1}\mathbf{B}_{r4}$.

$$\begin{aligned}&\det\left(\mathbf{Y}_{C2}(s)+\mathbf{Y}_{g4}(s)\right)=\det\left(\mathbf{S}_{GFM}\otimes\mathbf{Z}_{GFM}^{-1}(s)+\mathbf{B}_{r4}\otimes\mathbf{F}(s)\right)\\&=\det\left(\mathbf{S}_{GFM}\right)\cdot\prod_{j=1}^{m}\det\left(\mathbf{Z}_{GFM}^{-1}(s)+\sigma_j\mathbf{F}(s)\right)=0\end{aligned} \tag{14}$$

The simplified treatment of subsystem 1 is presented in 2).

2) Effect of the power synchronization control on GFL

In contrast to subsystem 2, subsystem 1 cannot be fully decoupled into multiple single-converter-infinite-bus systems, where each GFL converter is connected to the grid through an admittance. This is due to the structural difference between the admittance matrix $\mathbf{Y}_{C2}(s)$ and the line admittance matrix $\mathbf{Y}_{grid}(s)$. According to (2), since $Z_{dq}(s)$ remains nearly constant at Z_{dqm} for frequencies above 20 Hz [22], the inner-loop impedance $Z_{dq}(s)\boldsymbol{\alpha}(s)$ exhibits a form analogous to the impedance of transmission lines as expressed in (7). Further examining the synchronization impedance $\mathbf{Z}_{\mathrm{PF}}(s)$, it is desirable to approximate its influence on the GFL converters using a symmetric impedance $Z_{pf,eq}(s)\boldsymbol{\alpha}(s)$. The following proposition provides an approximate equivalence for $\mathbf{Z}_{\mathrm{PF}}(s)$.

Proposition II.2: The influence of $\mathbf{Z}_{\mathrm{PF}}(s)$ on the small-signal stability of GFL can be approximated by the impedance matrix $Z_{pf,eq}(s)\boldsymbol{\alpha}(s)$, where the equivalent synchronous impedance $Z_{pf,eq}(s)$ is given by:

$$Z_{pf,eq}(s)=\frac{\omega_0^2Z_{pf}}{2\left(s^2+\omega_0^2\right)}=\frac{\omega_0^3V_{d0}^2}{2\left(s^2+\omega_0^2\right)\left(Js^2+Ds\right)} \tag{15}$$

where Z_{pf} is the nonzero element in $\mathbf{Z}_{\mathrm{PF}}(s)$.

proof: See Appendix B.

The equivalent synchronous impedance $Z_{pf,eq}(s)$ varies as a function of frequency, with its Bode diagram depicted in Fig. 3(a). Within the frequency range prone to GFL instability (10–50 Hz), the phase of $Z_{pf,eq}(s)$ approaches 180° opposite to that of Z_{dq}, while the magnitude increases as the inertia coefficient J decreases. This observation can also be inferred from the expression of $Z_{pf,eq}(s)$, since when J is not too small and the frequency exceeds 10 Hz, the term Js^2 dominates in Js^2+Ds, resulting in a phase of 180°. Consequently, a smaller J results in a lower overall impedance of the GFM converter, making it more closely resemble a voltage source, thereby enhancing the stability of the GFL. This relationship is further corroborated by the GFL-dominated eigenvalues locus presented in Fig. 3(b).

This article has been accepted for publication in IEEE Transactions on Power Systems. This is the author's version which has not been fully edited and content may change prior to final publication. Citation information: DOI 10.1109/TPWRS.2026.3670426

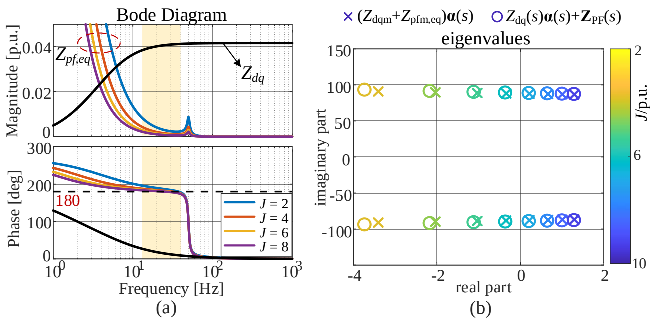

Fig. 3 (a) Bode diagram of the equivalent synchronous impedance; (b) Dominant eigenvalues locus

To obtain the conservative stability condition for GFL, this paper adopts the maximum value of the equivalent synchronous impedance $Z_{pf,eq}(s)$ within a frequency range to approximate its wideband characteristics. The equivalent GFM impedance is then approximated by $Z_{\mathrm{GFM}}\boldsymbol{\alpha}(s)$, which is expressed as:

$$Z_{GFM}=Z_{dqm}+Z_{pfm,eq}(J)$$
$$Z_{dqm}=\frac{\omega_0 L_f}{K_{pv}K_{pc}},\ Z_{pfm,eq}(J)=-\frac{\omega_0^3 V_{d0}^2}{2\sqrt{J^2\omega_1^4+D^2\omega_1^2}\left(\omega_0^2-\omega_1^2\right)} \quad (16)$$

where ω_1 represents an oscillatory frequency of the GFL, which is determined by its control parameters. The value of ω_1 can be obtained either through numerical computation or experimental measurement. In the numerical approach, ω_1 corresponds to the root of the algebraic equation given in (17).

$$\det\left(\mathbf{Y}_{GFL}(j\omega_1)\mathbf{F}(j\omega_1)+\lambda\mathbf{I}_2\right)=0 \quad (17)$$

where λ is an unknown real number. By decomposing (17) into its real and imaginary components, two algebraic equations are obtained, from which the oscillation frequency ω_1 can be explicitly determined.

Fig. 3(b) illustrates the effect of approximating the GFM impedance $Z_{\mathrm{GFM}}\boldsymbol{\alpha}(s)$ in place of $\mathbf{Z}_{\mathrm{GFM}}(s)$ on the GFL-dominated eigenvalues. This method maintains a conservative design approach while achieving satisfactory accuracy.

Similarly, when the GFM employs Q-V droop control, the effect of $\mathbf{Z}_{\mathrm{PF}}(s)+\mathbf{Z}_{\mathrm{QV}}(s)$ can be approximated by $Z_{pq,eq}(s)\boldsymbol{\alpha}(s)$, and $Z_{pq,eq}(s)$ denotes the equivalent power impedance.

$$Z_{pq,eq}(s)=\frac{\omega_0^2\left[\left(Z_{pf}-Z_{qv}\right)Z_{dqm}-Z_{pf}Z_{qv}\right]}{2\left(s^2+\omega_0^2\right)Z_{dqm}} \quad (18)$$

where Z_{qv} is the nonzero element in $\mathbf{Z}_{\mathrm{QV}}(s)$. The derivation procedure of (18) is identical to that of (15). Moreover, the wideband characteristic of $Z_{pq,eq}(s)$ is approximated by its maximum value within a specified frequency band for conservativeness.

Thus, $\mathbf{Y}_{g,eq}(s)$ in (12) can be approximated as the transfer function matrix of a resistive-inductive network, which characterizes the network features following the configuration of the GFM. Similar to subsystem 2, subsystem 1 can be approximately decoupled into multiple single-converter systems, where the grid-connected admittances correspond to the eigenvalues of matrix $\mathbf{S}_{\mathrm{GFL}}^{-1}\mathbf{B}_{\mathrm{Lred}}$.

$$\mathbf{Y}_{g,eq}(s)\approx\underbrace{\left[\mathbf{B}_{r1}-\mathbf{B}_{r2}\left(\mathbf{B}_{r4}+\Delta\mathbf{B}\right)^{-1}\mathbf{B}_{r3}\right]}_{\mathbf{B}_{Lred}}\otimes\mathbf{F}(s)$$
$$\Delta\mathbf{B}=\mathbf{S}_{GFM}\Big/\left(Z_{dqm}+Z_{pfm,eq}(J)\right) \quad (19)$$

It should be noted that regardless of the control strategy and parameters of the GFL converters, the eigenvalues of $\mathbf{S}_{\mathrm{GFL}}^{-1}\mathbf{B}_{\mathrm{Lred}}$ can reflect the grid strength of the system after the configuration of the GFM. This is of significant importance for assessing the stability of the GFL.

3) Stability characteristic of the GFL and GFM converters

Based on the studies in 1) and 2), the hybrid converter system can be approximated by partitioning and decoupling into multiple single-converter-infinite-bus systems. The stability problem of the original system is thus reduced to the stability analysis of individual GFL and GFM converters. A brief description of the stability characteristics of a single GFL and GFM converter is provided as follows.

The stability of the GFL converter diminishes as the grid admittance decreases. Therefore, the GFL remains stable when the smallest eigenvalue of matrix $\mathbf{S}_{\mathrm{GFL}}^{-1}\mathbf{B}_{\mathrm{Lred}}$ exceeds $\lambda_{GFL,C}$, where $\lambda_{GFL,C}$ represents the admittance required for the GFL to achieve critical stability. In the case of heterogeneous GFLs, $\lambda_{GFL,C}=\max_{i=1,\ldots,n}\{\lambda_{GFL,Ci}\}$, where $\lambda_{GFL,Ci}$ denotes the critical grid admittance for the *i*-th GFL converter.

In contrast to GFL, the stability of the GFM converter weakens as the grid admittance increases [31]. According to (14), the eigenvalues of $\mathbf{S}_{\mathrm{GFM}}^{-1}\mathbf{B}_{r4}$ must be smaller than the grid admittance $\lambda_{GFM,C}$, which ensures the critical stability of the GFM to guarantee its stability. The critical grid admittances $\lambda_{GFL,C}$ and $\lambda_{GFM,C}$ are both solely dependent on the control strategy and parameters of the converters.

III. Formulation of the Stability Constrained GFM ESS Configuration Problem

This section establishes the optimization configuration framework for GFM converters to enhance system stability. Specifically, for a given power system integrating multiple GFL-based renewable energy plants, the objective is to determine the optimal placement, capacity, and inertia of GFM ESS. The configuration must satisfy constraints on small-signal stability and rate of change of frequency while minimizing the overall investment cost.

A. System Stability Constraints

1) Small-signal stability constraint of GFL

The stability constraints of the multi-converter system encompass both GFL and GFM stability requirements. As analyzed in Section II.B, the stability constraint for GFL is given by:

$$\lambda_{\min}\left(\mathbf{S}_{GFL}^{-1}\mathbf{B}_{Lred}\right)\geq\lambda_{GFL,C} \quad (20)$$

where $\lambda_{\min}(\cdot)$ denotes the smallest eigenvalue of the matrix. Parameter $\lambda_{GFL,C}$ can be obtained through numerical modeling or experimental testing of a single GFL converter. A more straightforward approach is to adopt an empirical value. The

This article has been accepted for publication in IEEE Transactions on Power Systems. This is the author's version which has not been fully edited and content may change prior to final publication. Citation information: DOI 10.1109/TPWRS.2026.3670426

physical interpretation of $\lambda_{GFL,C}$ corresponds to the short-circuit ratio (SCR) at which a grid-connected GFL converter reaches critical stability, typically ranging between 2 and 3. For a conservative estimation, a value of 3 is often chosen, representing the boundary between strong and weak grids. If, after configuring the GFM based on $\lambda_{GFL,C} = 3$, the GFL remains unstable, this indicates that the equipment design is inadequate, rendering it unsuitable for grid connection.

2) Small-signal stability constraint of GFM

Since the inertia coefficient J of the GFM plays a crucial role in both small-signal stability and frequency stability of the power system, it is also considered an optimization variable in this study. The impact of J on GFL stability is reflected in its influence on the equivalent impedance of the GFM, as described in (16). Furthermore, J affects the stability of the GFM by altering the critical grid admittance $\lambda_{GFM,C}$. The stability constraint for the GFM converter is derived as follows, with the characteristic equation of the single GFM converter given by:

$$\begin{gathered}\det\left(Z_{dq}(s)\boldsymbol{\alpha}(s)+\boldsymbol{Z}_{PF}(s)+\sigma\boldsymbol{\alpha}(s)\right)=0\\ \left(\frac{s^2}{\omega_0^2}+1\right)\left(\frac{\omega_0 L_f}{H_V(s)}+\sigma\right)+\frac{\omega_0 V_{d0}^2}{Js^2+Ds}=0\end{gathered}\tag{21}$$

where σ is the grid impedance. Within the frequency range of GFM synchronization instability (10–20Hz), (21) satisfies $s^2/\omega_0^2 \ll 1$, allowing it to be neglected.

After simplification, (21) reduces to a quartic equation:

$$\begin{aligned}&J\left(K_{pc}K_{pv}\sigma+X_f\right)s^4+\left[JK_{VC}\sigma+D\left(K_{pc}K_{pv}\sigma+X_f\right)\right]s^3\\&+\left(JK_{ic}K_{iv}\sigma+DK_{VC}\sigma+\omega_0 V_{d0}^2K_{pc}K_{pv}\right)s^2\\&+\left(DK_{ic}K_{iv}\sigma+\omega_0 V_{d0}^2K_{VC}\right)s+\omega_0 V_{d0}^2K_{ic}K_{iv}=0\end{aligned}\tag{22}$$

Assuming $V_{d0}^2 = 2/3$ and applying Routh criterion, the stability condition for GFM is:

$$\begin{aligned}&\frac{\left[JK_{VC}\sigma+D\left(K_{pc}K_{pv}\sigma+X_f\right)\right]\omega_0K_{ic}K_{iv}}{b_1}\le\frac{3}{2}DK_{ic}K_{iv}\sigma+\omega_0K_{VC}\\&b_1=-\frac{J\left(K_{pc}K_{pv}\sigma+X_f\right)\left(DK_{ic}K_{iv}\sigma+2\omega_0K_{VC}/3\right)}{JK_{VC}\sigma+D\left(K_{pc}K_{pv}\sigma+X_f\right)}\\&\quad+JK_{ic}K_{iv}\sigma+DK_{VC}\sigma+2\omega_0K_{pc}K_{pv}/3\end{aligned}\tag{23}$$

After simplification, the stability criterion for a unit-capacity GFM converter is:

$$\begin{aligned}&\frac{2\omega_0K_{iv}K_{ic}}{3}f_1(\sigma)+\frac{J\left(K_{pv}K_{pc}\sigma+X_f\right)}{f_1(\sigma)}-\left(JK_{iv}K_{ic}+DK_{VC}\right)\sigma\\&-2\omega_0K_{pv}K_{pc}/3\le 0\end{aligned}\tag{24}$$

$$f_1(\sigma)=\frac{JK_{VC}\sigma+D\left(K_{pv}K_{pc}\sigma+X_f\right)}{DK_{iv}K_{ic}\sigma+2\omega_0K_{VC}/3}$$

where $X_f = \omega_0 L_f$, $K_{VC} = K_{pv}K_{ic} + K_{pc}K_{iv}$, and the physical quantities are expressed in per-unit values. The critical grid impedance σ_C of the GFM is defined as the value of σ that satisfies equality in (24). Consequently, (24) also provides an implicit function between critical grid impedance σ_C and the inertia coefficient J. Additionally, σ_C and the critical grid admittance $\lambda_{GFM,C}$ exhibit a reciprocal relationship.

With changes in the GFM control strategy, the functional relationship between σ_C and J is modified accordingly. The stability constraint of the GFM converters remains:

$$\lambda_{\max}\left(\mathbf{S}_{GFM}^{-1}\mathbf{B}_{r4}\right)\le 1/\sigma_C(J)\tag{25}$$

where $\lambda_{\max}(\cdot)$ denotes the biggest eigenvalue of the matrix. The relationship between $\sigma_C(J)$ and J is given by (24).

3) Inertia constraint

As power electronic devices replace the mechanical rotors of SGs, the system inertia is reduced, which may lead to excessive rates of change of frequency (RoCoF) under power fluctuations. This phenomenon is particularly pronounced in a power electronics-dominated power system. As a result, GFM converters are required to provide a certain level of inertia support, which imposes specific constraints on their inertia coefficient. For the sake of simplicity, this paper employs the maximum RoCoF as an indicator of the system's inertia, which typically occurs at the instant of the disturbance. According to the frequency response model in [32], the initial RoCoF, when subjected to a power step disturbance, is expressed as:

$$\left.\frac{df(t)}{dt}\right|_{t=0^+}=\frac{f_0\Delta P_L}{J_{SG}+J_{GFL}+J\sum_{i=1}^m S_{GFM,i}}\tag{26}$$

where f_0 is the rated frequency of the system, ΔP_L represents the power disturbance, J_{SG} and J_{GFL} correspond to the inertia of synchronous generators and GFL devices in the system. When GFL converters do not employ virtual inertia control, equation $J_{GFL} = 0$ holds. Otherwise, the effective inertia contributed by GFLs must be evaluated using other methods, which is beyond the scope of this paper (see [33] for reference).

From (26), the inertia constraint of the system can be derived as follows:

$$J\sum_{i=1}^m S_{GFM,i}\ge\frac{f_0\Delta P_L}{\dot{f}_{\lim}}-J_{SG}-J_{GFL}=J_{sys}\tag{27}$$

where $\dot{f}_{lim}$ is the maximum allowable RoCoF.

B. Description of the Optimization Problem

In practical scenarios, it is infeasible to deploy a GFM ESS at each renewable energy site. Therefore, the configuration strategy is considered to involve the installation of at most $N_{\max}$ GFM ESS (where $N_{\max} < n$) at a subset of n potential nodes. Given that this problem encompasses the siting of GFMs, the configuration problem can be formulated as the following MIP problem:

$$\text{(P1)}\qquad \min \mathrm{C}\left(\mathbf{S}_{GFM}\right)=\sum_{i=1}^n c_i S_{GFM,i}\tag{28}$$

Subject to (20), (25), (27),

$$\begin{cases} u_i S_{GFM}^{\min} \le S_{GFM,i} \le u_i S_{GFM}^{\max} \\ \sum_{i=1}^{n} u_i \le N_{\max} \\ u_i \in \{0,1\}, \quad i \in \{1,2,\cdots,n\} \end{cases} \tag{29}$$

where the objective function C($\mathbf{S}_{GFM}$) represents the total configuration cost of the GFM, with c_i denoting the cost of configuring a unit-capacity GFM. The binary variable $u_i = 1$ indicates the installation of a GFM at node i, while $u_i = 0$ signifies the absence of a GFM at node i. $S_{GFM}^{\max}$ and $S_{GFM}^{\min}$ represent the upper and lower capacity limits for the GFM.

The optimization problem (P1) takes into account different network topologies and converter control strategies, making it applicable to the GFM configuration of any system. Unlike conventional small-signal stability constraints based on dominant pole damping ratios, this study provides conditions that the network must satisfy to maintain converter stability. This approach not only avoids complex numerical calculations but also remains feasible when the internal structure and parameters of the converter are unavailable. Additionally, a detailed consideration of the GFM converter is provided. First, the impact of its inertia on the system's support capacity is quantified, which helps clarify the multifaceted influence of inertia on the system and enhances the accuracy of the GFM configuration results. Second, stability constraints specific to the GFM converter are established. Although GFM converters exhibit relatively good stability in weak grids with high renewable energy penetration, their capacity is generally much smaller than that of GFL converters, resulting in a relatively stronger grid from the GFM perspective. Specific case studies are presented in Section V.

C. The Relationship Between ESS Configurations with Different Objectives

The primary and most fundamental role of ESS is to maintain power balance in the power system. Most configurations are designed with energy management as the primary objective, such as peak shaving, frequency regulation, and reactive power support [14], [15]. Owing to its specific control structure, GFM ESS can not only provide these services but also offer support at shorter time scales, namely small-signal stability enhancement and inertia support, which are the focus of this study. These aspects precisely correspond to the challenges that must be addressed in renewable power systems. Although the configuration objectives differ, the proposed configuration for improving small-signal stability and inertia does not conflict with configurations aimed at energy management; instead, they can be integrated into a unified and comprehensive scheme.

The small-signal stable and inertia support investigated in this study occur at an ultra-short time scale (on the order of milliseconds). Thus, the energy capacity of ESS is not within the scope of consideration. From the perspective of energy management, system operators may determine the energy capacity, since the objective functions of long-term optimization typically include total rated power and energy capacity. Moreover, such studies seldom consider the placements of ESS, as their impact on the objective function is relatively minor. Consequently, the placement optimized in this work is unlikely to conflict with placements determined by other configuration objectives. On the other hand, the external characteristic of GFM ESS is only marginally affected by its output power [23]. Therefore, the power requirements imposed from the perspective of energy management do not compromise the maintenance of small-signal stability.

When optimizing the rated power of GFM ESS, both energy services and stability support must be taken into account, with the rated power determined as the larger of the two optimization outcomes. In summary, the optimized placement and rated power capacity of storage obtained in this work can serve respectively as a reference scheme and a necessary condition for power system planning, while the energy capacity should be determined according to energy management requirements.

IV. Proposed Method for Optimizing the Placement and Capacity of GFM ESS

This section presents a solution method for the GFM configuration problem (P1). Since the two eigenvalue constraints in (P1), namely (20) and (25), cannot be solved using existing solvers, different relaxation methods are employed to transform them into conventional constraints. Additionally, the complexity of the expression in (24) and the relatively low efficiency of simultaneously optimizing inertia and capacity pose challenges. To address this issue, a capacity-inertia two-layer iterative algorithm is proposed to improve the solution efficiency.

A. Relaxation of the Eigenvalue Constraints

1) Stability constraint of GFL

Assuming the inertia of the GFM is known, the matrix $\mathbf{S}_{\mathrm{GFL}}^{-1}\mathbf{B}_{\mathrm{Lred}}$ represents a complex decision variable dependent on the capacity of GFM. Let $\mathbf{A}(\mathbf{S}_{\mathrm{GFM}})=\mathbf{S}_{\mathrm{GFL}}^{-1/2}\mathbf{B}_{\mathrm{Lred}}\mathbf{S}_{\mathrm{GFL}}^{-1/2}$ denote a symmetric matrix; since $\mathbf{A}=\mathbf{S}_{\mathrm{GFL}}^{1/2}(\mathbf{S}_{\mathrm{GFL}}^{-1}\mathbf{B}_{\mathrm{Lred}})\mathbf{S}_{\mathrm{GFL}}^{-1/2}$ and $\mathbf{S}_{\mathrm{GFL}}^{-1}\mathbf{B}_{\mathrm{Lred}}$ are similar matrices, they share identical eigenvalues.

The second-order Taylor expansion of the multivariable function $\lambda_{\min}(\mathbf{A}(\mathbf{S}_{\mathrm{GFM}}))$ around the results of the k-th iteration is given by [24]:

$$\begin{aligned} \lambda_{\min}\left(\mathbf{A}\left(\mathbf{S}_{GFM}\right)\right) &= \lambda_{\min}^{(k)} + \left(\nabla\lambda_{\min}^{(k)}\right)^T \left(\mathbf{S}_{GFM} - \mathbf{S}_{GFM}^{(k)}\right) \\ &\quad + \frac{1}{2!}\left(\mathbf{S}_{GFM} - \mathbf{S}_{GFM}^{(k)}\right)^T \mathbf{H}\left(\mathbf{S}_{GFM,\theta}\right)\left(\mathbf{S}_{GFM} - \mathbf{S}_{GFM}^{(k)}\right) \\ \mathbf{S}_{GFM,\theta} &= \mathbf{S}_{GFM}^{(k)} + \theta\left(\mathbf{S}_{GFM} - \mathbf{S}_{GFM}^{(k)}\right) \quad \theta \in (0,1) \end{aligned} \tag{30}$$

where superscript (k) denotes the physical quantities generated at the k-th iteration, ∇ represents the gradient operator, and $\mathbf{H}(\cdot)$ is the Hessian matrix of the scalar function $\lambda_{\min}(\mathbf{A}(\mathbf{S}_{\mathrm{GFM}}))$. Noting the properties of the quadratic form, (30) can be further simplified as:

$$\lambda_{\min}\left(\mathbf{A}\right) \ge \lambda_{\min}^{(k)} + \left(\nabla\lambda_{\min}^{(k)}\right)^T \left(\mathbf{S}_{GFM} - \mathbf{S}_{GFM}^{(k)}\right) + \frac{\gamma}{2}\left\|\mathbf{S}_{GFM} - \mathbf{S}_{GFM}^{(k)}\right\|^2 \tag{31}$$

where $\gamma < \lambda_{\min}(\mathbf{H}(\mathbf{S}_{\mathrm{GFM},\theta}))$ is a tuning parameter and can be initially set to a smaller value and then adjusted based on the

This article has been accepted for publication in IEEE Transactions on Power Systems. This is the author's version which has not been fully edited and content may change prior to final publication. Citation information: DOI 10.1109/TPWRS.2026.3670426

convergence behavior.

$\nabla\lambda_{\min}^{(k)}$ is a column vector composed of the partial derivatives of $\lambda_{\min}(\mathbf{A}(\mathbf{S}_{\mathrm{GFM}}))$ with respect to each element of $\mathbf{S}_{\mathrm{GFM}}$:

$$\nabla\lambda_{\min}^{(k)}=\left[\frac{\partial\lambda_{\min}\left(\mathbf{A}\left(\mathbf{S}_{GFM}^{(k)}\right)\right)}{\partial S_{GFM,i}}\quad\cdots\quad\frac{\partial\lambda_{\min}\left(\mathbf{A}\left(\mathbf{S}_{GFM}^{(k)}\right)\right)}{\partial S_{GFM,n}}\right]^T \quad (32)$$

$$\frac{\partial\lambda_{\min}\left(\mathbf{A}\left(\mathbf{S}_{GFM}^{(k)}\right)\right)}{\partial S_{GFM,i}}=\mathbf{x}_1^T\frac{\partial\mathbf{A}\left(\mathbf{S}_{GFM}^{(k)}\right)}{\partial S_{GFM,i}}\mathbf{x}_1 \quad i\in\{1,2,\cdots n\} \quad (33)$$

where $\mathbf{x}_1$ and $\mathbf{x}_1^{\mathrm{T}}$ are the left and right eigenvectors of matrix $\mathbf{A}(\mathbf{S}_{\mathrm{GFM}})$ corresponding to the eigenvalue $\lambda_{\min}^{(k)}$, and

$$\begin{aligned}&\partial\mathbf{A}\left(\mathbf{S}_{GFM}^{(k)}\right)\Big/\partial S_{GFM,i}=\mathbf{S}_{GFL}^{-1/2}\mathbf{B}_{ac}\mathbf{E}_{n,i}\mathbf{B}_{ac}^T\mathbf{S}_{GFL}^{-1/2}\Big/Z_{GFM}\\&\mathbf{B}_{ac}=\mathbf{B}_{r2}\left(\mathbf{B}_{r4}+\Delta\mathbf{B}\left(\mathbf{S}_{GFM}^{(k)}\right)\right)^{-1}\end{aligned} \quad (34)$$

where $\mathbf{E}_{n,i}$ denotes an n-dimensional diagonal matrix with its ii-th diagonal element set to 1, while all other elements are zero.

In conclusion, in the neighborhood of $\mathbf{S}_{\mathrm{GFM}}^{(k)}$, the eigenvalue function $\lambda_{\min}(\mathbf{A}(\mathbf{S}_{\mathrm{GFM}}))$ can be approximated by the simplified expression on the right-hand side of (31). Accordingly, the constraint in (20) can be reformulated as:

$$\lambda_{\min}^{(k)}+\left(\nabla\lambda_{\min}^{(k)}\right)^T\left(\mathbf{S}_{GFM}-\mathbf{S}_{GFM}^{(k)}\right)+\frac{\gamma}{2}\left\|\mathbf{S}_{GFM}-\mathbf{S}_{GFM}^{(k)}\right\|^2\geq\lambda_{GFL,C} \quad (35)$$

2) Stability constraint of GFM

Given that the constraint in (25) pertains to the maximum eigenvalue of matrix $\mathbf{S}_{\mathrm{GFM}}^{-1}\mathbf{B}_{\mathrm{r4}}$, which is a diagonally dominant matrix, a relaxation approach based on matrix norms can be considered:

$$\lambda_{\max}\left(\mathbf{S}_{GFM}^{-1}\mathbf{B}_{r4}\right)\leq\left\|\mathbf{S}_{GFM}^{-1}\mathbf{B}_{r4}\right\|_\infty=\max_{i=1,2,\cdots,n}\left(\sum_{j=1}^{n}\left|\frac{B_{r4,ji}}{S_{GFM,j}}\right|\right) \quad (36)$$

where $\|\cdot\|_\infty$ represents the ℓ_∞-norm of the matrix, while $B_{r4,ji}$ represents the element located at the (j, i) position in matrix $\mathbf{B}_{r4}$.

It is noteworthy that when the optimized capacity of certain GFMs is 0, (36) becomes invalid. Therefore, the GFM stability constraint is reformulated as:

$$\left\|\mathbf{U}\left(\mathbf{S}_{GFM}+\delta\mathbf{I}_n\right)^{-1}\mathbf{B}_{r4}\right\|_\infty\leq 1\big/\sigma_C\left(J\right) \quad (37)$$

where $\mathbf{U}$ = diag$\{u_1,u_2,\ldots,u_n\}$, and δ represents a sufficiently small constant. When $S_{GFM,i}$ = 0 in the optimal solution, the i-th diagonal element of matrix $\mathbf{U}(\mathbf{S}_{\mathrm{GFM}}+\delta\mathbf{I}_n)^{-1}$ is zero. Equation (37) outlines the constraints for the non-zero GFM capacities.

B. The Capacity-Inertia Two-Layer Iterative Algorithm

To enhance the efficiency of solving the MIP problem (P1), this section introduces a two-layer iterative algorithm for capacity and inertia optimization. The inner layer focuses on capacity optimization, where the degenerate problem (P2) is solved based on the inertia coefficient provided by the outer layer, and the results are transmitted to the outer layer. The outer layer pertains to inertia optimization, where the inertia coefficient is updated based on the capacity optimization outcomes from the inner level, continuing until both the GFM capacity and inertia converge. The formulation of the degenerate optimization problem (P2) is given as follows:

$$\text{(P2)} \qquad \min \mathrm{C}\left(\mathbf{S}_{GFM}\right)=\sum_{i=1}^{n}c_iS_{GFM,i} \quad (38)$$

Subject to (29),

$$\begin{cases}\lambda_{\min}\left(\mathbf{S}_{GFL}^{-1}\mathbf{B}_{Lred}\right)\geq\lambda_{GFL,C}\\ \left\|\mathbf{U}\left(\mathbf{S}_{GFM}+\delta\mathbf{I}_n\right)^{-1}\mathbf{B}_{r4}\right\|_\infty\leq 1\big/\sigma_C\left(J^{(m)}\right)\end{cases} \quad (39)$$

where $J^{(m)}$ represents the inertia value provided by the outer layer optimization at the m-th iteration. The solution method for (P2) is first introduced.

Based on the aforementioned relaxation of the eigenvalue constraints, the optimization problem (P2) can be iteratively solved by addressing the sub-optimization problem (SubP2). Since the optimization problem (SubP2) is convex, it guarantees the existence of an optimal solution.

$$\text{(SubP2)} \qquad \min \mathrm{C}\left(\mathbf{S}_{GFM}\right)=\sum_{i=1}^{n}c_iS_{GFM,i} \quad (40)$$

Subject to (35), (37), (29).

Specifically, in each iteration, the optimization problem (SubP2) is solved. The result of the k-th iteration is used as the parameter $\mathbf{S}_{\mathrm{GFM}}^{(k+1)}$ for the next iteration, while parameter $\mathbf{S}_{\mathrm{GFM}}^{(k)}$ is derived from the solution of the optimization problem in the (k−1)-th iteration. The parameter $\mathbf{S}_{\mathrm{GFM}}^{(1)}$ in the first iteration is a given feasible initial value, ensuring that all constraints in (SubP2) are satisfied. The iterative process continues until the two sets of capacities are sufficiently close, i.e.:

$$\left\|\mathbf{S}_{GFM}^{(k+1)}-\mathbf{S}_{GFM}^{(k)}\right\|\leq\varepsilon_1 \quad (41)$$

where $\|\cdot\|$ represents the Euclidean norm of the vector, and $\varepsilon_1>0$ is the convergence threshold.

Based on the previous analysis, it is evident that when the inertia coefficient of the GFM decreases, both its own stability and the stability of the GFL (within the synchronous frequency range) improve, which results in a lower value for the objective function of (P2). Since in (P1), only constraint (27) limits the reduction of the GFM inertia, when (P1) reaches its optimal solution, constraint (27) must hold with equality. Therefore, the outer iteration can update the inertia value as follows:

$$J^{(m+1)}=\frac{1}{r}\left(J^{(m)}+(r-1)\frac{J_{sys}}{\left\|\mathbf{S}_{GFM}\right\|_1}\right) \quad (42)$$

where r > 1 is a tunable parameter, m denotes the number of outer iterations, and $\|\cdot\|_1$ represents the ℓ_1-norm. Similarly, the initial value for the outer iteration is a small inertia $J^{(1)}$, and the convergence criterion is given by $\|J^{(m+1)}$-$J^{(m)}\|<\varepsilon_2$.

In summary, the overall process of the proposed two-layer iterative algorithm for solving the optimization problem (P1) is shown in Fig. 4. The fundamental idea is to transform the original problem into two interlinked degenerate problems, with the outer iteration circumventing the nonlinear constraints of the original problem. Furthermore, for the degenerate problem (P2), the inner iteration relaxes the eigenvalue constraints and approximates the complex implicit function using piecewise simple functions. The entire optimization

This article has been accepted for publication in IEEE Transactions on Power Systems. This is the author's version which has not been fully edited and content may change prior to final publication. Citation information: DOI 10.1109/TPWRS.2026.3670426

process only requires the repeated solution of the MIP problem (SubP2), which can be efficiently solved using the Gurobi solver in MATLAB.

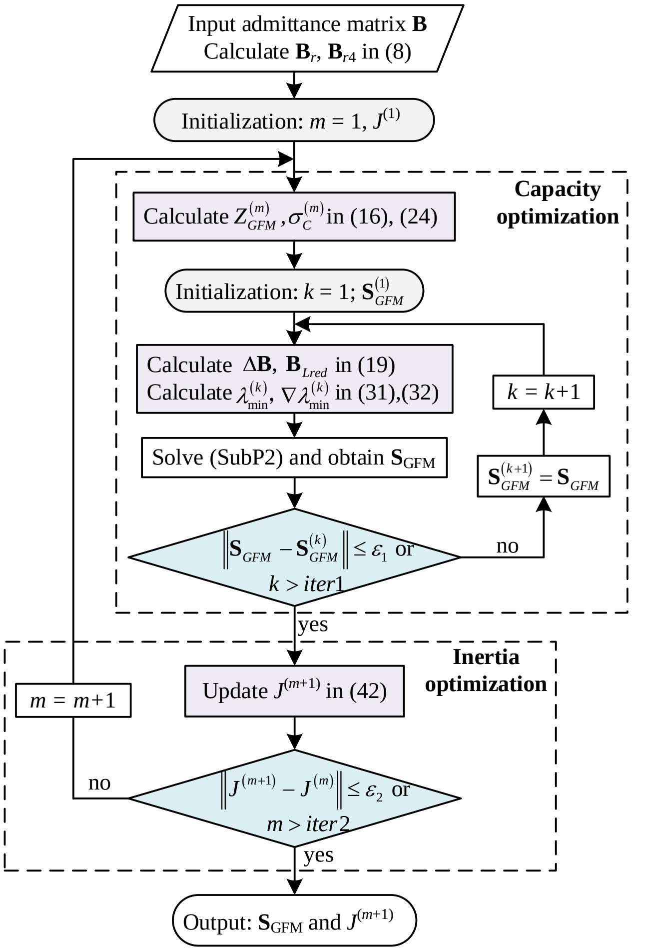

Fig. 4 Procedure of the proposed two-layer iterative algorithm

Lemma 3.5 in [34] establishes the convergence of the inner iteration. For the outer iteration, since the total capacity of GFM increases with each iteration, it follows from (42) that:

$$0 \ge J^{(m+1)} - \frac{J_{sys}}{\left\|\mathbf{S}_{GFM}^{(m)}\right\|_1} = \frac{1}{r}\left(J^{(m)} - \frac{J_{sys}}{\left\|\mathbf{S}_{GFM}^{(m)}\right\|_1}\right) \ge \frac{1}{r}\left(J^{(m)} - \frac{J_{sys}}{\left\|\mathbf{S}_{GFM}^{(m-1)}\right\|_1}\right) \tag{43}$$

$$\lim_{m\to\infty}\left|J^{(m+1)} - \frac{J_{sys}}{\left\|\mathbf{S}_{GFM}^{(m)}\right\|_1}\right| \le \lim_{m\to\infty}\frac{1}{r^{m-1}}\left|J^{(2)} - \frac{J_{sys}}{\left\|\mathbf{S}_{GFM}^{(1)}\right\|_1}\right| = 0 \tag{44}$$

This proves the convergence of the two-layer iterative algorithm. Lemma 3.6 of [34] presents the optimality condition and proves that the convergent value of $\mathbf{S}_{\mathrm{GFM}}$ also satisfies this condition, thereby guaranteeing the optimality of the algorithm. On this basis, the optimality condition of the proposed model is given by:

$$\begin{cases} \exists\mu > 0,\ \mathbf{U}\mathbf{c} = \mu\cdot\mathbf{U}\nabla\lambda_{\min}\left(\mathbf{A}\left(\mathbf{S}_{GFM}^{*}\right)\right) \\ \lambda_{\min}\left(\mathbf{A}\left(\mathbf{S}_{GFM}^{*}\right)\right) = \lambda_{GFL,C} \end{cases} \tag{45}$$

where $\mathbf{c} = [c_1, \ldots, c_n]^{\mathrm{T}}$. Equation (45) can be used to verify the optimality of the optimization results, which will be demonstrated in the case study.

V. Case Study

In this section, the proposed GFM configuration method is applied to a modified IEEE 39-bus system, with electromagnetic transient simulations in MATLAB/Simulink conducted to validate the effectiveness of the configuration results. Additionally, considering the potential future scenario in which certain power systems may operate with 100% renewable energy penetration, a case study on a fully inverter-based power system is presented to demonstrate the general applicability of the proposed method.

In the modified IEEE 39-bus system depicted in Fig. 5, GFL renewable energy units are connected at buses 1–9, while the SG is located at bus 39. The candidate buses for GFM deployment are {11,15,19,28,29,31,34,38,10}. Based on empirical data, GFM ESS are integrated into the designated buses via transformers with an impedance of 0.06 p.u. The unit capacity configuration cost is defined as c_i = 1p.u., i = 1,2,…,9. The network line parameters remain consistent with those in [29], and the control parameters of the converters can be found in Appendix C.

A. Case Study on the Modified IEEE 39-Node System

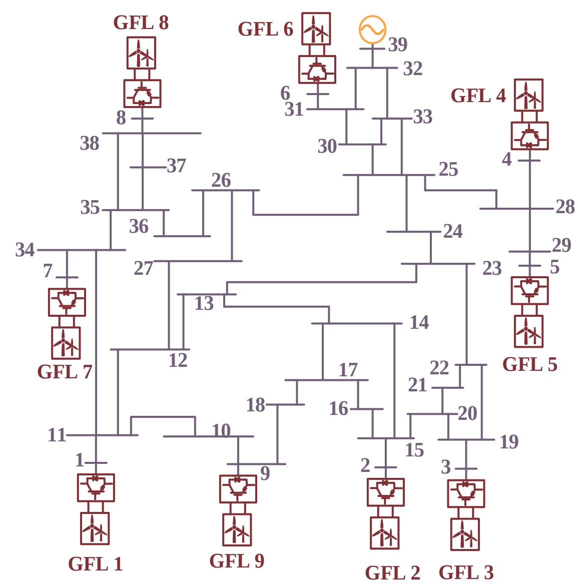

Fig. 5 Diagram of the modified IEEE 39-bus system

To reduce grid strength, the capacity matrix of the GFL converters is defined as $\mathbf{S}_{\mathrm{GFL}}$ = diag{2, 2, 2, 1, 1, 1, 2.5, 2.5, 3}. Based on the control parameters, the critical grid admittance required for stability is determined as $\lambda_{GFL,C}$=3.03. Under these conditions, the minimum eigenvalue of matrix $\mathbf{S}_{\mathrm{GFL}}^{-1}\mathbf{B}_{\mathrm{Lred}}$ is computed as 1.58, indicating that the system is unable to maintain the stability of the GFL converters.

1) Convergence and optimality analysis of the algorithm

This article has been accepted for publication in IEEE Transactions on Power Systems. This is the author's version which has not been fully edited and content may change prior to final publication. Citation information: DOI 10.1109/TPWRS.2026.3670426

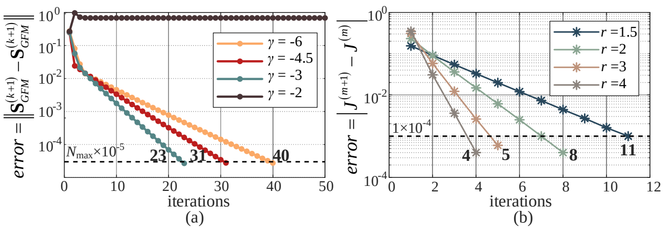

Fig. 6 Algorithm convergence speed under different parameter settings. (a) inner-layer iterations; (b) outer-layer iterations

The convergence of the proposed algorithm is first validated. In this case study, the tolerance values are set as $\varepsilon_1 = N_{\max}\times10^{-5}$ and $\varepsilon_2 = 10^{-4}$. Taking $N_{\max} = 3$ as an example, Fig. 6(a) illustrates the variation of capacity error with iteration count during the first round of inner-layer iterations, where the vertical axis is presented in a logarithmic scale. It can be observed that the convergence rate of the inner iteration increases as the parameter γ grows; however, when $\gamma > -2$, the algorithm diverges. Additionally, as shown in Fig. 6(b), the convergence rate of the outer iteration accelerates with increasing parameter r. When both γ and r are appropriately selected, the inner and outer iterations achieve rapid convergence.

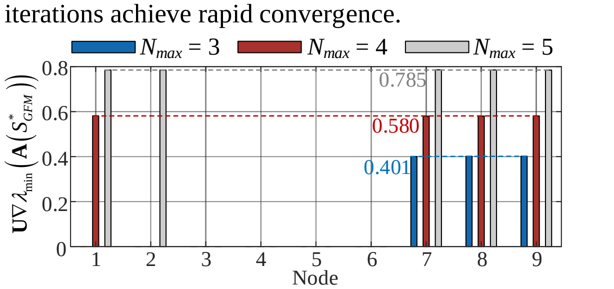

Fig. 7 Gradient calculation results at the optimal solution.

When the algorithm converges, the gradient computation results under different values of $N_{\max}$ are illustrated in Fig. 7. Verification shows that these results satisfy the condition specified in (45), thereby ensuring their optimality.

Furthermore, TABLE I presents the time consumptions and iterations of the algorithm for $N_{\max} = 3$ under varying numbers of candidate nodes. The second column reports the total number of possible GFM placement combinations. As the number of candidate nodes increases, the total iteration count remains nearly unchanged, thereby demonstrating the applicability of the proposed method to systems of different scales.

TABLE I
TIME CONSUMPTIONS AND ITERATIONS WITH $N_{\max} = 3$

Number of candidate nodes	Combinations	Time/s	Iterations
3	1	11.71	52
5	25	15.83	52
9	129	25.09	53

2) Comparison of configuration results for different quantities of GFMs

Based on the proposed two-layer iterative algorithm, the configuration results for different allowable quantities of GFMs, $N_{\max} = 3, 4, 5$, are presented in TABLE II. When $N_{\max} = 3$, the optimal GFM placement is determined near buses 7, 8, and 9. As $N_{\max}$ increases, GFMs are also deployed on buses 1 and 2, leading to a reduction in configuration costs. Notably, when $N_{\max}$ is further increased, the optimal solution remains identical to the case of $N_{\max} = 5$. To explain this phenomenon, TABLE III summarizes the active constraints corresponding to the optimal solutions in the three cases. The results indicate that when $N_{\max} = 3$ or 4, the capacity allocated to each individual GFM is relatively large, and the GFM stability constraint (37) is not activated. However, when $N_{\max} = 5$, the stability constraint of the GFMs becomes active, imposing a lower bound on the capacity of each GFM and preventing further cost reduction.

TABLE II
CONFIGURATION RESULTS OF DIFFERENT ALLOWABLE QUANTITIES

$N_{\max}$	$\mathbf{S}_{\mathrm{GFM}}$/p.u.	J/p.u.	$C(\mathbf{S}_{\mathrm{GFM}})$
3	[0, 0, 0, 0, 0, 0, 0.532 0.477 0.691]	2.353	1.700
4	[0.325, 0, 0, 0, 0, 0, 0.327, 0.325, 0.465]	2.774	1.442
5	[0.292, 0.271, 0, 0, 0, 0, 0.286, 0.263, 0.313]	2.808	1.425

TABLE III
ACTIVE CONSTRAINT UNDER DIFFERENT ALLOWABLE QUANTITIES

$N_{\max}$	Difference of (20)	Difference of (37)
3	1.6×10^{-7}	40.30
4	2.5×10^{-7}	7.51
5	0.08	-1.18×10^{-7}

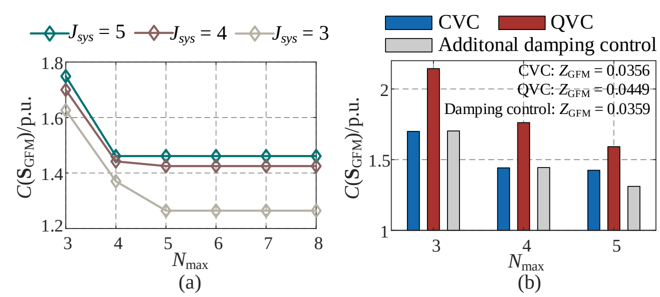

Fig. 8 Total cost of GFM configuration. (a) with different inertia requirements; (b) with different control strategies.

Furthermore, Fig. 8(a) presents the minimum configuration cost under different inertia requirements and varying values of $N_{\max}$. The results indicate that as the upper limit of allowable GFM configurations increases, the configuration cost decreases, eventually stabilizing. Additionally, when the inertia requirements of the system increase, the total GFM capacity for configuration increases, while the optimal quantity of GFMs decreases. For instance, when $J_{sys} = 5$, the optimal quantity of GFMs reduces to 4. This result suggests that decentralized GFM configurations can reduce investment costs to some extent; however, the effectiveness of this reduction is constrained by stability considerations.

3) Comparison of configuration results for different control strategies of GFMs

The control strategies of the GFM influence the configuration results through two pathways. Specifically, they modify the external characteristics of GFM, thereby affecting its support to GFL converters; this effect is reflected in the equivalent impedance Z_{GFM}. In addition, the control strategies can also alter the critical grid impedance σ_C. To further illustrate these effects, Q–V droop control and additional damping control are considered in this subsection, and the corresponding configuration results are summarized in TABLE IV.

TABLE IV
CONFIGURATION RESULTS OF DIFFERENT GFM CONTROL STRATEGIES

Control	$N_{\max}$	$\mathbf{S}_{\mathrm{GFM}}$/p.u.	J/p.u.	$C(\mathbf{S}_{\mathrm{GFM}})$

Q-V droop	3	[0, 0, 0, 0, 0, 0, 0.671, 0.601, 0.871]	1.865	2.144
	4	[0.396, 0, 0, 0, 0, 0, 0.400, 0.397, 0.569]	2.270	1.762
	5	[0.284, 0.284, 0, 0, 0, 0, 0.293, 0.309, 0.422]	2.514	1.592
Additional damping control	3	[0, 0, 0, 0, 0, 0, 0.533, 0.477, 0.692]	2.349	1.703
	4	[0.326, 0, 0, 0, 0, 0, 0.327, 0.325, 0.466]	2.771	1.444
	5	[0.247, 0.231, 0, 0, 0, 0, 0.241, 0.250, 0.341]	3.051	1.311

As $N_{\max}$ increases, the total configuration cost decreases under all three control strategies, while noticeable differences among the strategies are observed, as shown in Fig. 8(b). When Q–V droop control is adopted, the equivalent impedance of the GFM increases from 0.0356 p.u. to 0.0449 p.u., resulting in a higher required capacity to ensure sufficient grid strength. In contrast, under additional damping control, the equivalent impedance of the GFM exhibits no significant change, whereas the critical grid impedance σ_C is reduced, thereby improving the intrinsic stability of the converter. Consequently, when $N_{\max}$ = 5, the adoption of additional damping control can further reduce the configuration cost.

In summary, Q–V droop control and additional damping control influence the configuration results by modifying the external characteristics of the GFM and its intrinsic stability threshold, respectively. Achieving desirable external characteristics and stability of the GFM within specific frequency ranges constitutes one effective approach for providing precise grid support.

4) Simulation validation of the configuration results

The accuracy of the configuration results is validated through electromagnetic simulations. Taking the results for $N_{\max}$ = 3 as an example, Fig. 9 shows the output power responses of the converters after a voltage sag lasting 0.02 seconds, applied at 2 seconds. Subplots (a), (b), and (c) correspond to settings 1, 2, and 3 in TABLE V, respectively. In all conditions, the configuration of GFM capacity and placement is consistent with the results in TABLE II.

TABLE V
PARAMETER SETTINGS AND THEORETICAL CALCULATION RESULTS

Settings	J/p.u.	K_{pc}/p.u.	$\lambda_{\min}(\mathbf{S}_{\mathrm{GFL}}^{-1}\mathbf{B}_{\mathrm{Lred}})$	$\lambda_{GFL,C}$
1	2.382	0.23	3.04	3.03
2	2.382	0.2	3.04	3.12
3	1.2	0.2	3.18	3.12

As illustrated in Fig. 9(a), since $\lambda_{\min}\left(\mathbf{S}_{\mathrm{GFL}}^{-1}\mathbf{B}_{\mathrm{Lred}}\right)\approx\lambda_{GFL,C}$, the power responses of the converters exhibit nearly equal-amplitude oscillations following the disturbance. In (b), a reduction in the proportional gain K_{pc} of the GFL current control loop increases the critical stability admittance to $\lambda_{GFL,C}$ = 3.12>3.04, resulting in system instability. To further examine the impact of inertia on the small-signal stability of GFL converters, (c) reduces the inertia of the GFM to 1.2 p.u. Under these conditions, the value of $\lambda_{\min}\left(\mathbf{S}_{\mathrm{GFL}}^{-1}\mathbf{B}_{\mathrm{Lred}}\right)$ increases to 3.18, exceeding 3.12, thereby ensuring system stability. The theoretical predictions align with the time-domain simulation results, confirming the validity of the proposed analysis.

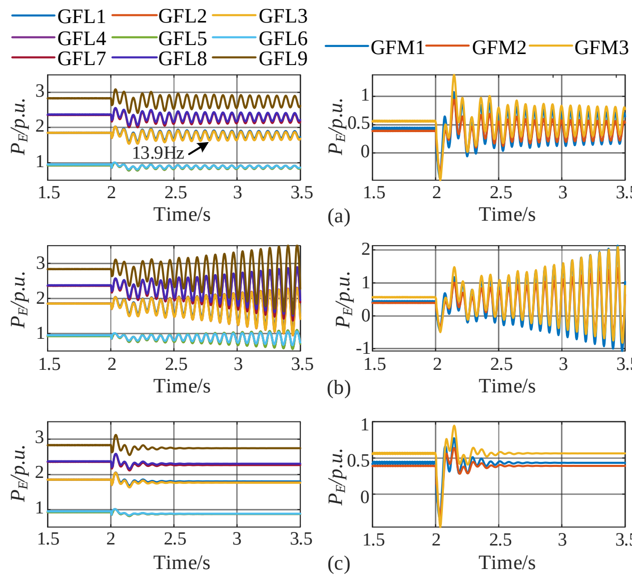

Fig. 9 Simulation results of different parameter settings. (a) Setting 1; (b) Setting 2; (c) Setting 3.

To illustrate potential stability issues arising from GFM deployment, this case study presents a comparison by providing configuration results without considering the GFM stability constraint, as shown in TABLE VI. The maximum allowable quantity of GFMs is set to $N_{\max}$ = 5. When the GFM stability constraint is not enforced, the total configuration cost is lower. However, stability analysis reveals that the constraint is violated, as $\lambda_{\max}(\mathbf{S}_{\mathrm{GFM}}^{-1}\mathbf{B}_{r4})$ = 69.12 > 58.05 = $1/\sigma(J)$. Fig. 10 presents simulation results for both configuration scenarios. When all constraints are considered, the system stabilizes following a disturbance. In contrast, when the GFM stability constraint is not enforced, the output power of the converters diverges, indicating system instability, with the oscillatory mode predominantly governed by the GFM. These simulation results validate the effectiveness of the proposed configuration method and highlight the necessity of incorporating the GFM stability constraint.

TABLE VI
CONFIGURATION RESULTS OF DIFFERENT CONSTRAINTS

Constraints	$\mathbf{S}_{\mathrm{GFM}}$/p.u.	J/p.u.	C($\mathbf{S}_{\mathrm{GFM}}$)
All constraints	[0.279, 0.261, 0, 0, 0, 0, 0.272, 0.250, 0.300]	2.936	1.362
Without constraint (37)	[0.232, 0.231, 0, 0, 0, 0, 0.237, 0.252, 0.344]	3.083	1.297

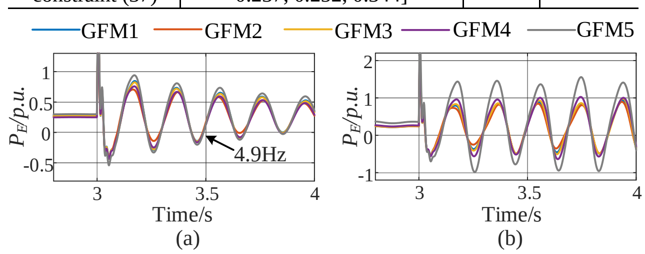

Fig. 10 Simulation results of different constraints. (a) All constraints; (b) Without the stability constraint of GFM

Finally, the configuration results under different control strategies of GFM are compared. Fig. 11(a) validates the configuration results when Q–V droop control (QVC) is considered. During the interval from 2s to 4s, the system

This article has been accepted for publication in IEEE Transactions on Power Systems. This is the author's version which has not been fully edited and content may change prior to final publication. Citation information: DOI 10.1109/TPWRS.2026.3670426

operates at the critical stability boundary. At t = 4s, the GFM switches to constant voltage control (CVC), after which the power outputs of all converters converge. These results confirm that the support capability of the GFM is weakened under Q–V droop control, which is consistent with the configuration results. In addition, Fig. 11(a) validates the configuration results when additional damping control is considered. During 2–4s, the GFM operates with additional damping control. At t = 4s, the additional damping control loop is removed, and the power trajectories of the converters evolve from a critically stable state to divergence. The simulation results also verify the effectiveness of additional damping control in enhancing the stability of the GFM.

In summary, the proposed configuration method is applicable to GFM control strategies under diverse grid requirements, thereby further demonstrating its generality.

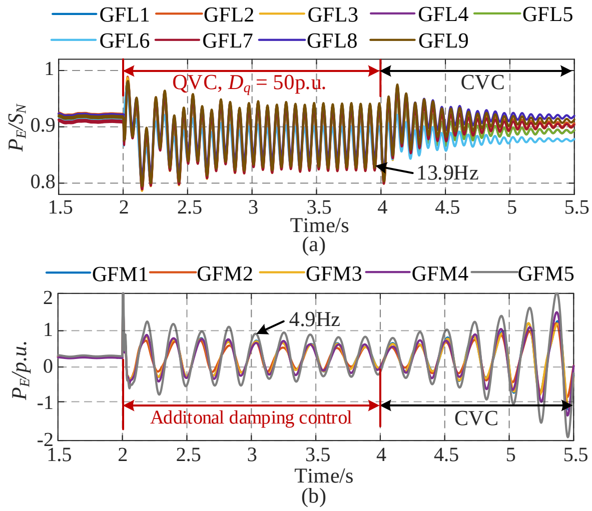

Fig. 11 Simulation results of different control strategies. (a) Q-V droop control; (b) additional damping control.

B. Case Study on a Fully Inverter-Based Power System

In a fully inverter-based power system, the absence of SG support necessitates the deployment of GFM converters with adequate capacity to ensure stability. In addition, since the system is disconnected from the main grid, frequency may exhibit significant fluctuations under disturbances, thereby making the consideration of inertia constraints essential. In the practical fully inverter-based system illustrated in Fig. 12, four GFL wind farms and multiple GFM ESS collectively form an independent system operating in islanded mode. While the available information does not allow for a precise determination of which GFL is more susceptible to instability, the proposed configuration method remains applicable.

The capacity matrix of the GFL converters is defined as $\mathbf{S}_{\rm GFL}$ = diag{1, 0.62, 0.42, 0.48}, with candidate buses for GFM deployment including all 35 kV and 110 kV buses (buses 5–10). The critical grid admittance $\lambda_{GFL,C}$ remains 3.03, the system power disturbance is set to 0.1 p.u., and the maximum allowable RoCoF is specified as 1Hz/s. The control parameters are consistent with those specified in part A.

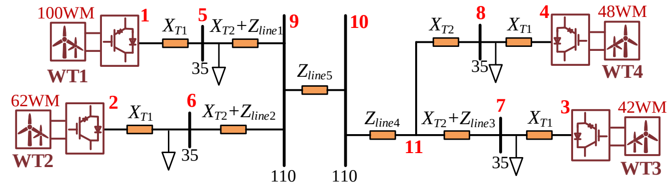

Fig. 12 Diagram of the fully inverter-based power system.

TABLE VII
CONFIGURATION RESULTS OF THE FULLY INVERTER-BASED SYSTEM

$N_{\max}$	Locations	$S_{\rm GFM}$/p.u.	J/p.u.	Cost
2	5, 6	0.377, 0.260	3.953	0.638
3	5, 6, 8	0.176, 0.114, 0.122	6.108	0.413
4	5, 6, 7, 8	0.147, 0.093, 0.066, 0.073	6.658	0.379

TABLE VII summarizes the GFM configuration results under different allowable quantities $N_{\max}$. Given the absence of an external grid, GFM converters do not encounter instability issues, resulting in a notable decrease in configuration costs as $N_{\max}$ increases. When $N_{\max} \geq 5$, the optimal solution to the optimization problem remains unchanged from the case of $N_{\max}$ = 4, indicating that a decentralized and locally optimized deployment of GFM converters can achieve improved economic efficiency. Moreover, the results of this case study offer an empirical reference: for a fully inverter-based power system operating in islanded mode, ensuring stable operation typically requires allocating approximately 15%–25% of the total system capacity to GFM converters.

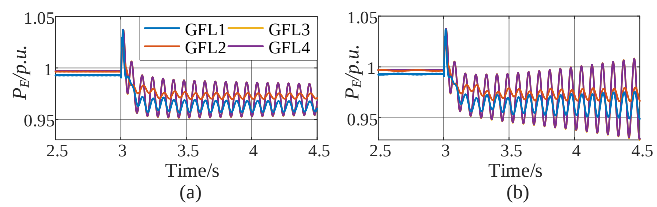

Fig. 13 Time-domain response of the GFL power under a line disturbance. (a) J = 3.953; (b) J = 6.000.

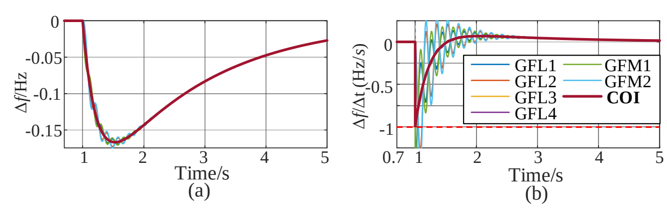

Fig. 14 Frequency responses of the converters and the COI frequency under a load step disturbance.

Fig. 13 presents the simulation validation of the configuration results for $N_{\max}$ = 2. To facilitate observation, the output power of each GFL is expressed as the ratio of its actual power to its rated power, and the impedance X_{line5} increases to 1.05X_{line5} at t = 3s. As shown in (a), when GFM converters are configured according to the optimization results, the system approaches critical stability following the line disturbance. In (b), an increase in GFM inertia coefficient leads to $\lambda_{\min}\left(\mathbf{S}_{\rm GFL}^{-1}\mathbf{B}_{\rm Lred}\right) < \lambda_{GFL,C}$, causing the power outputs of the converters to diverge.

The proposed configuration method not only guarantees small-signal stability but also limits large-scale frequency deviations. At t = 1 s, a 0.1 p.u. load step is applied at node 6, and the waveforms of the system (COI) frequency and its rate

This article has been accepted for publication in IEEE Transactions on Power Systems. This is the author's version which has not been fully edited and content may change prior to final publication. Citation information: DOI 10.1109/TPWRS.2026.3670426

of change are shown in Fig. 14. It can be observed that, under the proposed configuration, both the frequency and its rate of change stay within the permissible limits. These simulation results demonstrate the effectiveness of the proposed method.

VI. CONCLUSION

This paper proposes a configuration method for GFM ESS in hybrid power systems, incorporating small-signal and inertia constraints. The proposed method derives the equivalent stability conditions for the system, thereby formulating the configuration problem as a MIP problem. The proposed capacity-inertia two-layer iterative algorithm circumvents the eigenvalue constraints and complex nonlinear constraints, thereby improving computational efficiency. Case studies are conducted on the modified IEEE 39-bus system and a fully inverter-based system, where the proposed algorithm demonstrates good convergence properties and delivers accurate configuration results. The analysis of different allowable quantities of GFMs indicates that a more distributed GFM deployment can reduce investment costs to some extent; however, the quantity of GFMs and the associated cost are inherently constrained by stability requirements. Furthermore, it is proven that the configuration scheme is closely related to the control strategies and stability of the GFM converters. The proposed configuration method comprehensively accounts for multiple stability constraints, contributing to both cost-effective investments in modern power systems and enhanced operational stability.

APPENDIX A
PROOF OF PROPOSITION II.1

Proof: Based on the Schur complement transformation, for any block matrix, the following expression holds when $\mathbf{D}$ is invertible:

$$\det\left(\begin{bmatrix}\mathbf{A} & \mathbf{B}\\ \mathbf{C} & \mathbf{D}\end{bmatrix}\right)=\det(\mathbf{D})\cdot\det\left(\mathbf{A}-\mathbf{B}\mathbf{D}^{-1}\mathbf{C}\right) \tag{46}$$

Thus, the closed-loop characteristic equation (10) of the system can be rewritten as:

$$\begin{aligned}&\det\left(\begin{bmatrix}\mathbf{Y}_{C1}(s) & \\ & \mathbf{Y}_{C2}(s)\end{bmatrix}+\begin{bmatrix}\mathbf{Y}_{g1}(s) & \mathbf{Y}_{g2}(s)\\ \mathbf{Y}_{g3}(s) & \mathbf{Y}_{g4}(s)\end{bmatrix}\right)=0\\ &=\det\left(\mathbf{Y}_{C1}(s)+\underbrace{\mathbf{Y}_{g1}(s)-\mathbf{Y}_{g2}(s)\left[\mathbf{Y}_{C2}(s)+\mathbf{Y}_{g4}(s)\right]^{-1}\mathbf{Y}_{g3}(s)}_{\mathbf{Y}_{g,eq}(s)}\right)\\ &\quad\det\left(\mathbf{Y}_{C2}(s)+\mathbf{Y}_{g4}(s)\right)\\ &=\det\left(\mathbf{Y}_{C1}(s)\mathbf{Y}_{g,eq}^{-1}(s)+\mathbf{I}_{2n}\right)\cdot\det\left(\mathbf{Y}_{C2}(s)\mathbf{Y}_{g4}^{-1}(s)+\mathbf{I}_{2m}\right)\\ &\quad\det\left(\mathbf{Y}_{g,eq}(s)\right)\cdot\det\left(\mathbf{Y}_{g4}(s)\right)\end{aligned} \tag{47}$$

Since $\mathbf{Y}_{g,eq}(s)$ and $\mathbf{Y}_{g4}(s)$ do not possess any unstable poles, the unstable poles of the original system (i.e., the roots of the characteristic equation in the right-half plane) correspond to the union of the unstable poles of the two subsystems in (9). This completes the proof.

APPENDIX B
PROOF OF PROPOSITION II.2

Proof: By means of the Parallel GFL-GFM unit shown in Fig. 15, the effect of power synchronization control on the stability of GFL is analyzed. When Node i is disconnected from the external system, the characteristic equation of it is given by:

$$\begin{aligned}&\det\left(\mathbf{I}_2+\mathbf{Y}_{GFL}(s)\left(Z_{dqm}\boldsymbol{\alpha}(s)+\mathbf{Z}_{PF}(s)\right)\right)=0\\ &\left(\frac{s^2}{\omega_0^2}+1\right)Y_{dd}Y_{qq}Z_{dqm}^2+\left[\frac{s}{\omega_0}\left(Y_{dd}+Y_{qq}\right)+Y_{dd}Y_{qq}Z_{pf}\right]Z_{dqm}+1=0\end{aligned} \tag{48}$$

where Y_{dd} and Y_{qq} represent the diagonal elements of $\mathbf{Y}_{GFL}(s)$, and the non-diagonal elements can be ignored [30]. Z_{pf} is the nonzero element of $\mathbf{Z}_{PF}(s)$.

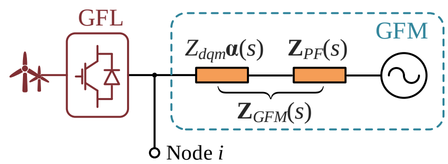

Fig. 15 Illustration of a Parallel GFL-GFM unit.

The objective is to identify a suitable $Z_{pf,eq}$ such that the roots of the following characteristic equation approximate those of (48).

$$\left(\frac{s^2}{\omega_0^2}+1\right)Y_{dd}Y_{qq}\left(Z_{dqm}+Z_{pf,eq}\right)^2+\frac{s}{\omega_0}\left(Y_{dd}+Y_{qq}\right)\left(Z_{dqm}+Z_{pf,eq}\right)+1=0 \tag{49}$$

The terms in (48) involving Z_{pf} can be regarded as perturbations, where $Z_{pf,eq}$ represents small variations induced by Z_{pf}. Expanding (49) and substituting (48) yields:

$$Z_{pf,eq}=\frac{\omega_0^2 Z_{pf}Y_{dd}Y_{qq}Z_{dqm}}{\underbrace{2\left(s^2+\omega_0^2\right)Y_{dd}Y_{qq}Z_{dqm}}_{den1}+\underbrace{s\omega_0\left(Y_{dd}+Y_{qq}\right)}_{den2}} \tag{50}$$

where the high-order term $Z_{pf,eq}^2$ is neglected.

Furthermore, Fig. 16 presents the Bode diagram of the denominator in (50) under typical parameter values. It can be observed that within the 10–30 Hz frequency range, the magnitude of den2 is much smaller than that of den1 and can be approximately neglected. Accordingly, the expression of the equivalent synchronous impedance is obtained as:

$$Z_{pf,eq}(s)\approx\frac{\omega_0^2 Z_{pf}}{2\left(s^2+\omega_0^2\right)} \tag{51}$$

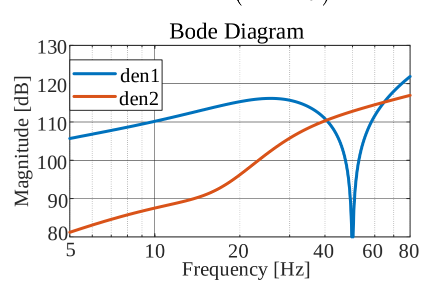

Fig. 16 Magnitude of the denominator in $Z_{pf,eq}$.

APPENDIX C
CONVERTERS CONTROL PARAMETERS

The control schemes of the GFL and GFM converters are consistent with those presented in [20], and the corresponding control parameters are summarized in TABLE VIII.

TABLE VIII
CONTROL PARAMETERS OF CONVERTERS IN THE IEEE 39-NODE SYSTEM

Base value for per-unit calculation		
f_{Base}=50Hz	S_{Base}=100MW	V_{Base}=380V
Control parameters of GFL converter (per-unit values)		
PLL controller	K_{ppll}, K_{ipll}	0.68, 35
Power controller	K_{pp}, K_{ip}	0.5, 40
Current controller	K_{pc}, K_{ic}	0.23, 10
Control parameters of GFM converter (per-unit values)		
APC controller	J, D	4, 50
RPC controller	D_q	50
Additional damping control	K_ω, T_w, T_1, T_2	10, 5, 0.3, 0.1
Voltage controller	K_{pv}, K_{iv}	4, 30
Current controller	K_{pc}, K_{ic}	0.3, 10

REFERENCES

[1] H. Holttinen et al., “Variable renewable energy integration: status around the world,” *IEEE Power Energy Mag*., vol. 19, no. 6, pp. 86–96, Nov. 2021.
[2] Q. Peng, Q. Jiang, Y. Yang, T. Liu, H. Wang, and F. Blaabjerg, “On the stability of power electronics-dominated systems: challenges and potential solutions,” *IEEE Trans. on Ind. Applicat*., vol. 55, no. 6, pp. 7657–7670, Nov. 2019.
[3] X. Wang, M. G. Taul, H. Wu, Y. Liao, F. Blaabjerg, and L. Harnefors, “Grid-synchronization stability of converter-based resources—An overview,” *IEEE Trans. Ind. Appl*., vol. 1, pp. 115–134, 2020.
[4] B. Wen, D. Boroyevich, and R. Burgos, P. Mattavelli, and Z. Shen, “Analysis of D-Q small-signal impedance of grid-tied inverters,” *IEEE Trans. Power Electron*., vol. 31, no. 1, pp. 675–687, Jan. 2016.
[5] D. Wu, G. Li, M. Javadi, A. M. Malyscheff, M. Hong, and J. N. Jiang, “Assessing impact of renewable energy integration on system strength using site-dependent short circuit ratio,” *IEEE Trans. Sustain. Energy*, vol. 9, no. 3, pp. 1072–1080, Jul. 2018.
[6] Y. Cheng et al., “Real-world subsynchronous oscillation events in power grids with high penetrations of inverter-based resources,” *IEEE Trans. Power Syst*., vol. 38, no. 1, pp. 316–330, Jan. 2023.
[7] Dan Liu, Qiufan Yang, Yin Chen, Xia Chen, and Jinyu Wen. “Optimal Parameters and Placement of Hybrid Energy Storage Systems for Frequency Stability Improvement,” Protect. Control Mod. Power Syst., vol. 10, no. 2, pp. 40-53, Mar. 2025.
[8] B. Pawar, E. I. Batzelis, S. Chakrabarti and B. C. Pal, “Grid-Forming Control for Solar PV Systems With Power Reserves,” *IEEE Trans. Sustain. Energy*, vol. 12, no. 4, pp. 1947-1959, Oct. 2021.
[9] K. Zhang, M. Shi, X. Chen, D. Shao, Y. Xu and Y. Chen, “Interaction Modeling and Stability Analysis of Grid-Forming Energy Storage System Based on SISO Transfer Functions,” *IEEE Trans. Sustain. Energy*, vol. 16, no. 1, pp. 573-587, Jan. 2025.
[10] Y. Teng, W. Deng, W. Pei, Y. Li, L. Dingv, and H. Ye, “Review on grid-forming converter control methods in high-proportion renewable energy power systems,” Global Energy Interconnection, vol. 5, no. 3, pp. 328–342, Jun. 2022.
[11] J. C. Hernandez, P. G. Bueno, and F. Sanchez-Sutil, “Enhanced utility scale photovoltaic units with frequency support functions and dynamic grid support for transmission systems,” *IET Renewable Power Gener*., vol. 11, no. 3, pp. 361–372, Jan. 2017.
[12] X. Wu, J. Zhao, and A. Conejo, “Optimal battery sizing for frequency regulation and energy arbitrage,” *IEEE Trans. Power Delivery*, vol. 37, no. 3, pp. 2016–2023, Jun. 2022.
[13] J. Li, Y. Xue, L. Tian and X. Yuan, “Research on Optimal Configuration Strategy of Energy Storage Capacity in Grid-Connected Microgrid,” *Prot. Control Mod. Power Syst.*, vol. 2, no. 4, pp. 1-7, October 2017.
[14] V. Knap, S. K. Chaudhary, D. -I. Stroe, M. Swierczynski, B. -I. Craciun and R. Teodorescu, “Sizing of an Energy Storage System for Grid Inertial Response and Primary Frequency Reserve,” *IEEE Trans. Power Syst*., vol. 31, no. 5, pp. 3447-3456, Sept. 2016.
[15] L. Tziovani, L. Hadjidemetriou, C. Charalampous, M. Tziakouri, S. Timotheou and E. Kyriakides, “Energy Management and Control of a Flywheel Storage System for Peak Shaving Applications,” *IEEE Trans. Smart Grid*, vol. 12, no. 5, pp. 4195-4207, Sept. 2021.
[16] B. Kroposki et al., “Achieving a 100% renewable grid: Operating electric power systems with extremely high levels of variable renewable energy,” *IEEE Power Energy Mag*., vol. 15, no. 2, pp. 61–73, Mar. 2017.
[17] L. Harnefors, X. Wang, A. G. Yepes, and F. Blaabjerg, “Passivity-based stability assessment of grid-connected VSC–an overview,” *IEEE J. Emerg. Sel. Topics Power Electron*., vol. 4, no. 1, pp. 116–125, Mar. 2016.
[18] Y. Zhou et al., “Small-signal stability assessment of heterogeneous grid-following converter power systems based on grid strength analysis,” *IEEE Trans. Power Syst*., vol. 38, no. 3, pp. 2566–2579, May 2023.
[19] P. Wang, J. Ma, R. Zhang, S. Wang, and T. Liu, “Configuration method of grid-forming converters to enhance multi-converter system stability,” *IEEE Trans. Power Electron*., vol. 39, no. 10, pp. 12743-12754, Oct. 2024.
[20] C. Yang, L. Huang, H. Xin, and P. Ju, “Placing grid-forming converters to enhance small signal stability of PLL-integrated power systems,” *IEEE Trans. Power Syst*., vol. 36, no. 4, pp. 3563–3573, Jul. 2021.
[21] H. Xin, C. Liu, X. Chen, Y. Wang, E. Prieto-Araujo, and L. Huang, “How many grid-forming converters do we need? a perspective from small signal stability and power grid strength,” *IEEE Trans. Power Syst*., vol. 40, no. 1, pp. 623-635, Jan, 2025.
[22] F. Ma, H. Xin, D. Wu, Y. Liu, and X. Chen, “Assessing small-signal grid strength of 100% inverter-based power systems,” *IEEE Trans. on Power Delivery*, vol. 39, no. 5, pp. 2784-2796, Oct. 2024.
[23] F. Zhao, X. Wang, Z. Zhou, et al., “Control Interaction Modeling and Analysis of Grid-Forming Battery Energy Storage System for Offshore Wind Power Plant,” *IEEE Trans. Power Syst*., vol. 37, no. 1, pp. 497-507, Jan. 2022.
[24] Y. Liu, Y. Chen, H. Xin, *et al*., “System Strength Constrained Grid-Forming Energy Storage Planning in Renewable Power Systems,” *IEEE Trans. Sustain. Energy*, vol. 16, no. 2, pp. 981-994, Apr. 2025.
[25] Y. Wang, J. Ma, C. Wang, *et al*., “Capacity Estimation Method of Grid-Forming Converters From the Perspective of Grid Strength,” *2023 3rd Power System and Green Energy Conference (PSGEC)*, Shanghai, China, 2023, pp. 1049-1053.
[26] L. Huang et al., “Grid-synchronization stability analysis and loop shaping for PLL-based power converters with different reactive power control,” *IEEE Trans. Smart Grid*, vol. 11, no. 1, pp. 501–516, Jan. 2020.
[27] Y. Li, Y. Gu, Y. Zhu, A. Junyent-Ferré, X. Xiang and T. C. Green, “Impedance Circuit Model of Grid-Forming Inverter: Visualizing Control Algorithms as Circuit Elements,” *IEEE Trans. Power Electron*., vol. 36, no. 3, pp. 3377-3395, March 2021.
[28] X. Xiong, X. Li, B. Luo, M. Huang, C. Zhao and F. Blaabjerg, “An Additional Damping Torque Method for Low-Frequency Stability Enhancement of Virtual Synchronous Generators,” *IEEE Trans. Power Electron.*, vol. 39, no. 12, pp. 15858-15869, Dec. 2024.
[29] L. Huang, D. Wang, X. Wang, et al., “Gain and phase: Decentralized stability conditions for power electronics-dominated power systems,” *IEEE Trans. Power Syst*., vol. 39, no. 6, pp. 7240-7256, Nov. 2024.
[30] C. Liu, H. Xin, D. Wu, et al., “Generalized operational short-circuit ratio for grid strength assessment in power systems with high renewable penetration,” *IEEE Trans. Power Syst*., vol 39, no. 4, pp. 5479-5494, Jul. 2024.
[31] F. Zhao, X. Wang and T. Zhu, “Power Dynamic Decoupling Control of Grid-Forming Converter in Stiff Grid,” *IEEE Trans. Power Electron*., vol. 37, no. 8, pp. 9073-9088, Aug. 2022.
[32] A. Venkatraman, U. Markovic, D. Shchetinin, E. Vrettos, P. Aristidou and G. Hug, “Improving Dynamic Performance of Low-Inertia Systems Through Eigensensitivity Optimization,” *IEEE Trans. Power Syst*., vol. 36, no. 5, pp. 4075-4088, Sept. 2021.
[33] G. Hu, Y. Yang, H. Xin, *et al*., “A Unified Method for Assessing Frequency Support Capability of Diverse Renewable Power Generation Units,” *IEEE Trans. Sustain. Energy*, doi: 10.1109/TSTE.2025.3584791.
[34] E. Mengi, “A support function based algorithm for optimization with eigenvalue constraints,” SIAM J. Optim., vol. 27, no. 1, pp. 246–268, Jan. 2017.

This article has been accepted for publication in IEEE Transactions on Power Systems. This is the author's version which has not been fully edited and content may change prior to final publication. Citation information: DOI 10.1109/TPWRS.2026.3670426

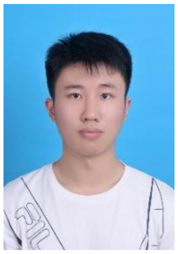

Kezan Zhang received the B.Eng. degree in electrical engineering in 2022 from the Huazhong University of Science and Technology, Wuhan, China, where he is currently working toward the Ph.D. degree in electrical engineering. His research interests include modeling and control technologies of energy storage system, and renewable energy stability analysis.

Xia Chen received the B.S. degree in power system and its automaton from Wuhan University of Technology, China, in 2006, and the M.S. and Ph.D. degrees in electrical engineering from Huazhong University of Science and Technology (HUST), China, in 2008 and 2012, respectively. She was a Post-Doctoral Research Fellow with the University of Hong Kong, from 2012 to 2015. Now she is a professor with the School of Electrical and Electronic Engineering, HUST. Her research interests include energy storage control and operation, renewable energy integration technologies, and new smart grid device.

Yin Chen received the B.S. degree in electrical engineering from Huazhong University of Science and Technology, Wuhan, China, in 2009, and the M.S. degree in electrical engineering from Zhejiang University, Hangzhou, China, in 2014. He received the Ph.D. degree in Electrical Engineering from University of Strathclyde, Glasgow, U.K., in 2020. He is currently a associate researcher with University of Strathclyde in Glasgow, UK. His research interests include modelling of power electronic converters, grid integration of renewable power, and stability analysis of the HVDC transmission systems.

Hui Yang received the B.Eng. and Ph.D. degrees from the School of Electrical and Electronic Engineering, Huazhong University of Science and Technology (HUST), Wuhan, China, in 2014 and 2021, respectively. From 2022 to 2025, she has been a Postdoctoral Research Associate with HUST. Her current research interests include dynamical system analysis of power system.

Huanhai Xin (Senior Member, IEEE) received the Ph.D. degree from the College of Electrical Engineering, Zhejiang University, Hangzhou, China, in June 2007. He was a Postdoctoral Researcher in the Department of Electrical Engineering and Computer Science, University of Central Florida, FL 32816, USA, from 2009 to 2010. He is currently a Professor with the College of Electrical Engineering, Zhejiang University. His research interests include renewable power system stability analysis and control. He was the recipient of the National Natural Science of China for Excellent Young Scholars.

Jinyu Wen received his B.Eng. and Ph.D. degrees all in electrical engineering from Huazhong University of Science and Technology (HUST), Wuhan, China, in 1992 and 1998, respectively. He was a Visiting Student from 1996 to 1997 and Research Fellow from 2002 to 2003 all at the University of Liverpool, Liverpool, UK, and a Senior Visiting Researcher at the University of Texas at Arlington, Arlington, USA, in 2010. From 1998 to 2002, he was a Director Engineer in XJ Electric Co. Ltd., Xuchang, China. In 2003, he joined the HUST and now is a Professor at HUST. His current research interests include renewable energy integration, energy storage application, DC grid, and power system operation and control.